

2022

Computational fluid dynamics optimisation of grid fin aerodynamic design for reusable launch vehicles

Orders, J.

Orders, J. (2022) 'Computational fluid dynamics optimisation of grid fin aerodynamic design for reusable launch vehicles', The Plymouth Student Scientist, 15(2), pp. 404-463.

<http://hdl.handle.net/10026.1/20110>

University of Plymouth

All content in PEARL is protected by copyright law. Author manuscripts are made available in accordance with publisher policies. Please cite only the published version using the details provided on the item record or document. In the absence of an open licence (e.g. Creative Commons), permissions for further reuse of content should be sought from the publisher or author.

Computational fluid dynamics optimisation of grid fin aerodynamic design for reusable launch vehicles

Jack Orders

*Project Advisor: [Adam Kyte](#), School of Engineering, Computing, and Mathematics
Faculty of Science and Engineering, University of Plymouth*

Abstract

Grid fins are an unconventional flight control surface utilised by SpaceX for its Falcon 9 reusable launch vehicle upon re-entry. Previous literature surrounding grid fins has used computational fluid dynamics (CFD) to investigate sensitivity factors of the design to vary drag or maximise hinge moment but often suffer from limitations (e.g., insufficient modelling of the boundary layer, or no evidence of sensitivity studies/validation). Due to the lack of literature a systematic CFD-based method is employed in which grid fin geometry is simplified to a 2D flat plate and validated against Tekure (2021) and the simulation verified using oblique shock wave theory (White, 2009; NACA and NASA, 2017). The method increases in complexity as it progresses to a 2D lattice and subsequently a 3D cell (1 portion of a grid fin), investigating the impact of plate spacing, thickness and material selection on the total drag and maximum temperature. In line with the presented methodology each simulation undergoes mesh and domain studies to ensure sufficient convergence of the solution and to certify independence of the solution. Subsequently a design is suggested that increases drag by 21.7% whilst maintaining the original designs measured maximum temperature. By considering the effects of the increased drag and varying the grid fin material, a simplified grid fin geometry is applied to analytical beam bending theory to provide an estimated factor of safety (FoS) and suggest the validity of composite integration.

Keywords: Computational fluid dynamics, grid fin, shockwaves, supersonic, validation, verification, independence study, ANSYS-CFX, ANSYS-Fluent, 2D flat plate, materials, design points, SpaceX

Introduction

Second only to safety factors, cost is the most essential criterion to ensure viability for any space flight operation. Since 2002, SpaceX (2022), an American aerospace company, has been developing a reusable first-stage rocket, Falcon 9, to reduce flight costs and maximise payload capacity. This reusable first stage utilises an unconventional flight control surface, known as a grid fin, to guide the rocket during high-speed atmospheric re-entry. These grid fins provide both attitude control and increase the drag profile of the first stage – slowing it as it descends.

The deployment of grid fins to the Space X fleet has increased the cost-effectiveness of flights and ultimately lead to the success of the Falcon 9 and rocket reusability – a revolutionary game-changing aerospace discovery. Figure 1 shown below, shows the extent of Falcon 9's impact on access to space.

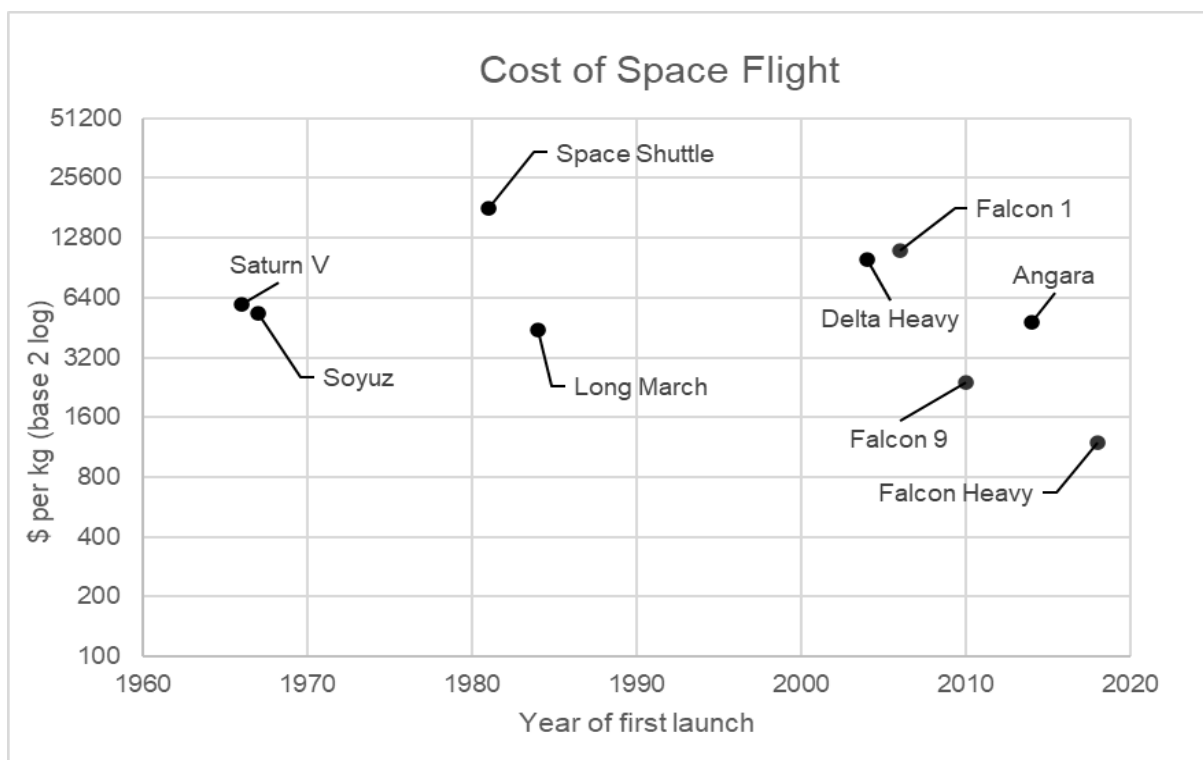


Figure 1: Evolution of space flight costs per kilogram from 1960-2020 (Venditti, 2022)

Whilst grid fins have caused a revolution in spaceflight they were initially designed for Soviet-era ballistic missiles as well as the N-1, the Soviet moon program rocket. Their initial mounting on rockets resulted in no need to gimbal engines for controllability and instead relied on the fins for attitude control, an inexpensive yet effective solution. Resultingly, they have seen many appearances on large modern munitions. In typical applications however, grid fins are often avoided due to their higher drag coefficient compared to conventional planar fins despite their superior control effectiveness. Such aerodynamic characteristics however make them a viable choice for launch vehicle recovery applications. Figure 2 below shows the velocity and altitude profile upon re-entry from a recent Falcon 9 mission, otherwise known as telemetry data (Shahar, 2020, and Space X, 2020). Such conditions require the fins to be operable throughout sub/trans and supersonic flow speeds. As well as a range of temperatures and pressures, whether it be ambient conditions at sea level, the cold vacuum of space or the high temperatures of re-entry.

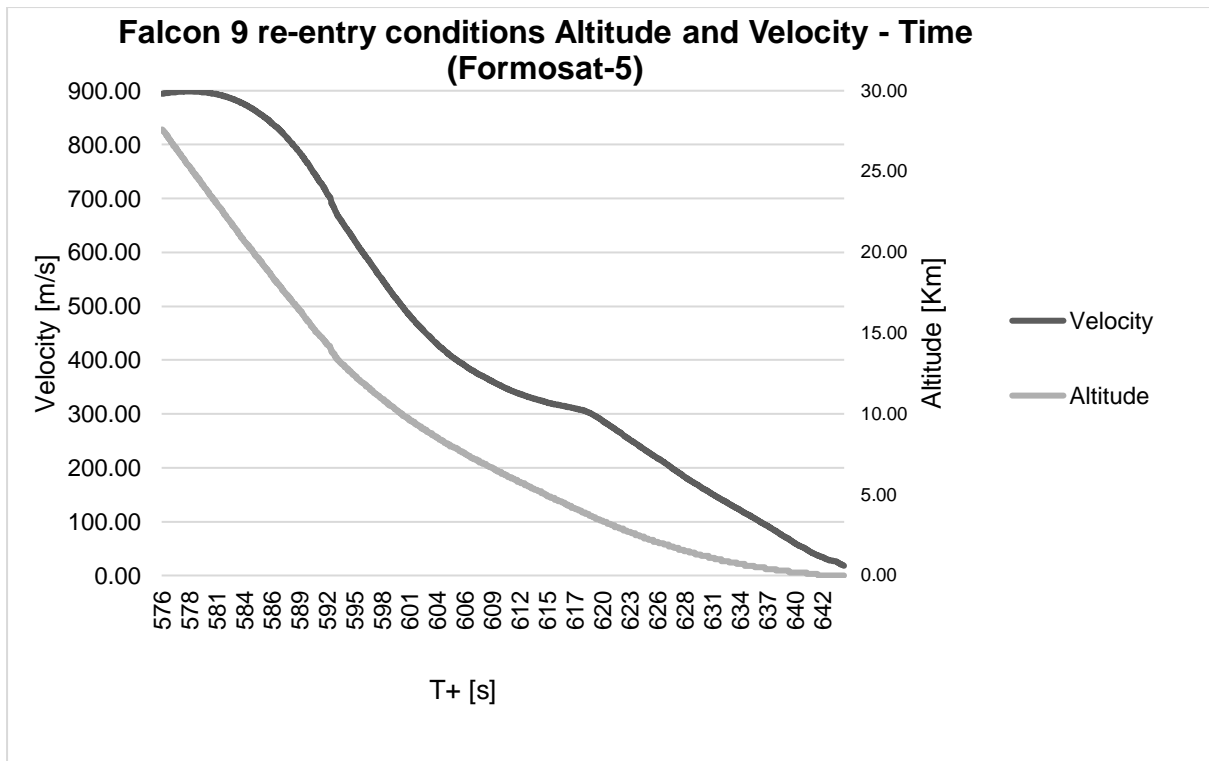


Figure 2: Falcon 9 re-entry altitude and velocity telemetry data from formosat-5 (Shahar and Space X, 2020)

Methodology

Overview

CFD is an incredibly powerful tool, but without validation and verification would provide an entirely meaningless solution. Selecting an appropriate methodology therefore is essential and is the backbone of this paper. Figure 3 (a) shows the basics of a CFD workflow, (b) shows the steps for achieving a reliable, validated, solution, and Figure 4 overleaf shows the project methodology.

These ideas of verification and validation are very similar and can often become confused. They are best defined as:

Validation – Determines if the simulation agrees with physical reality. Usually done by examining an existing DNS paper (Direct numerical simulation) or against experimental results.

Verification – Determines if the computational implementation of the model is correct, by comparing to exact analytical results.

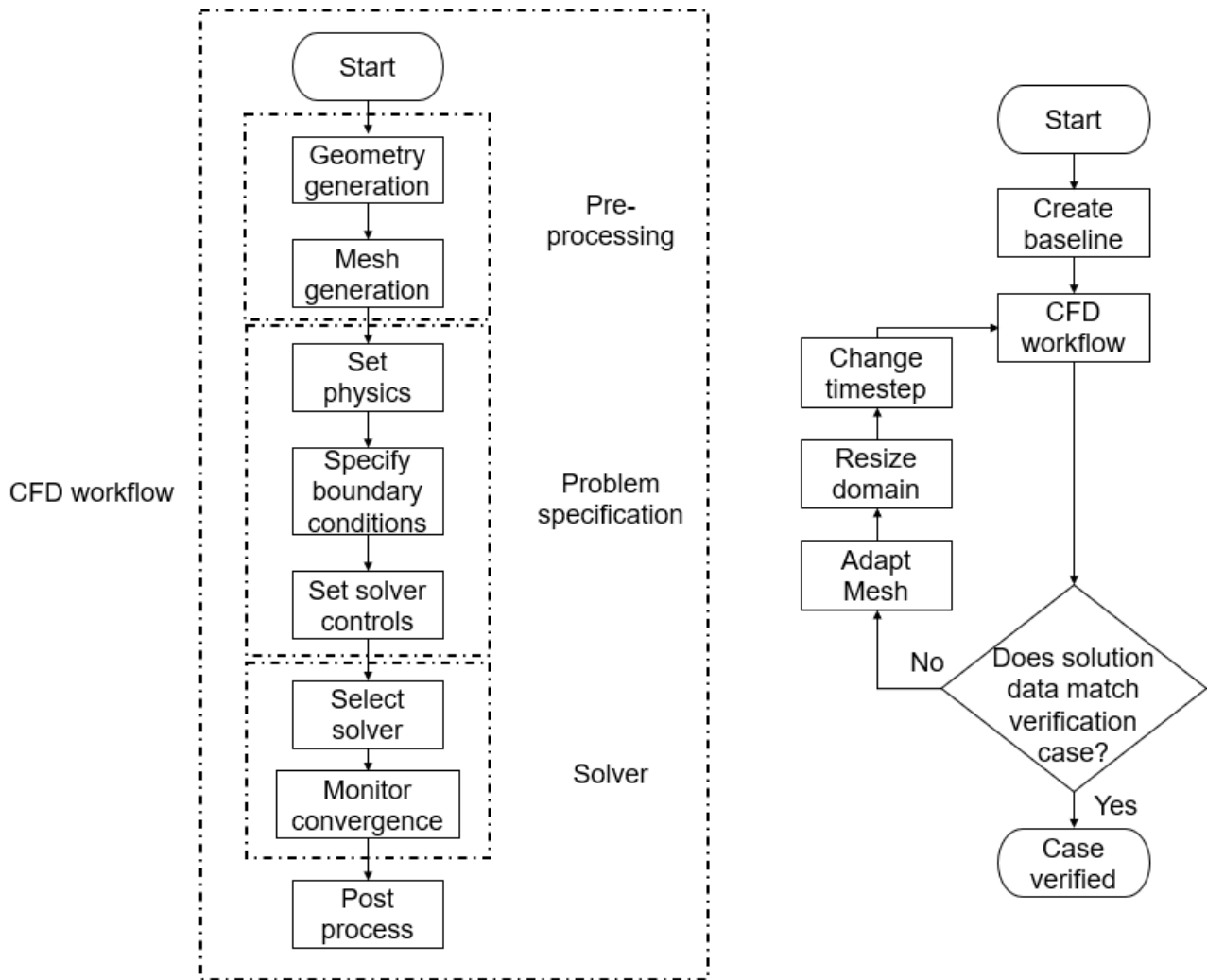


Figure 3: (a) Basic CFD workflow, and (b) validation and verification workflow

Project

Combining the CFD workflow of (a) with these methods of validation and verification (b) helps us to produce a workflow specific to this project and ensures that the results produced are as accurate as possible without the ability to directly verify them to experimental or analytical data.

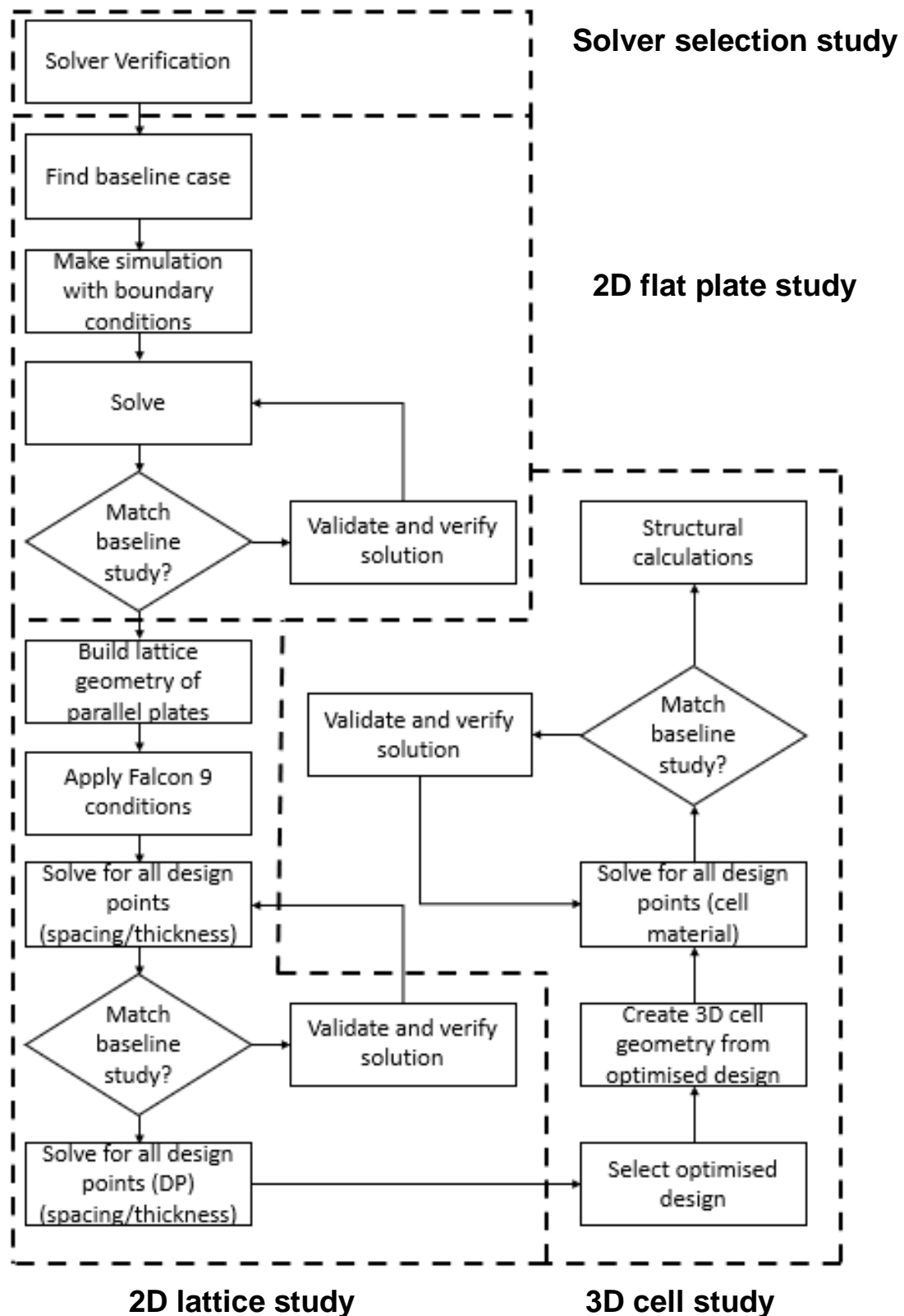


Figure 4: Workflow for papers CFD studies

Review of Literature

Fluid Mechanics – Theory of supersonic, compressible flow

To comprehend the complex fluid behaviour of high-velocity flows, commonplace assumptions regarding the physical properties of air under ambient conditions must be thrown out and concepts such as Mach number, density variation and heat transfer must be well understood. Consider a baseline case of a grid fin by simplifying it to the 2D plane and applying symmetry (a singular flat plate) moving through a volume of air, as shown in Figure 5. Truncating the real-world domain to this closed system allows us to only consider how the fluid interacts with itself and the plate.

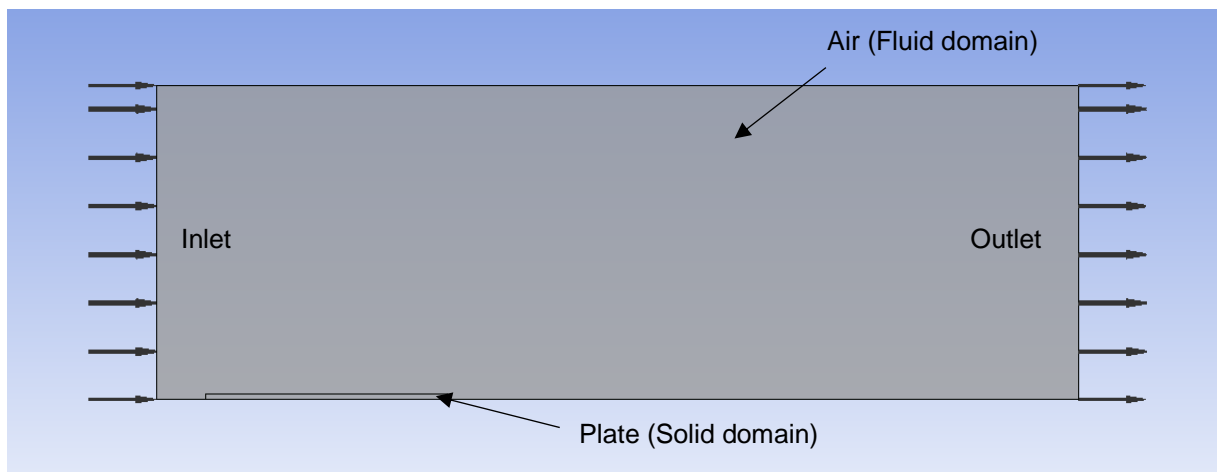


Figure 5: Simplified 2D case of a grid fin in a fluid domain

Fluid moving at high velocities, such as the air around Falcon 9, are subject to compressibility effects where the density of the fluid may vary locally as it's compressed by the object. While all fluids at any velocity are subject to some degree of compressibility, a mathematical assumption is introduced that flows, below Mach 0.3, are incompressible. Mach number refers to the dimensionless ratio determined by the velocity of an object in motion to the local speed of sound. Determination of the Mach number helps categorise the flow regime the body is present in. Figure 6, below, shows the name of each flow regime corresponding to the range of Mach number and the compressibility assumption (Chanson, 1996).

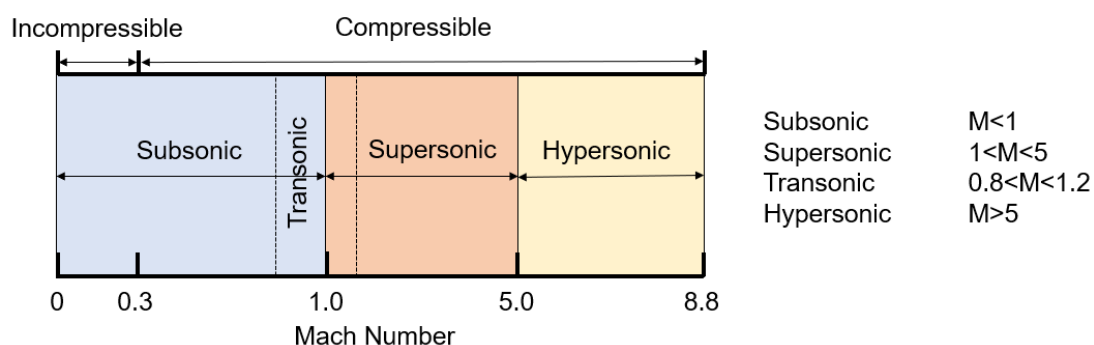


Figure 6: Flow regime corresponding to Mach number

These ideas of flow speed and fluid compressibility introduce the concept of shock waves. Shock waves are instantaneous yet discontinuous regions of flow that have vastly different thermo- and aero-dynamic properties to the free stream flow (Anderson, 2003; Blazek, 2005). Figure 7 overleaf (a, b, and c) represent various variables across a shock. The instantaneous, discontinuous change as shown in Figure 7 below cannot be ignored when using CFD methods. Measurements of shockwave thickness have resulted in values of approximately 200nm (Fox and McDonald, 1992). Therefore, for shocks to be accurately modelled in CFD, an extremely fine region of mesh would be required, which is computationally expensive and difficult to model (Modesti and Pirozzoli, 2016). The effect of this will be investigated in independency studies.

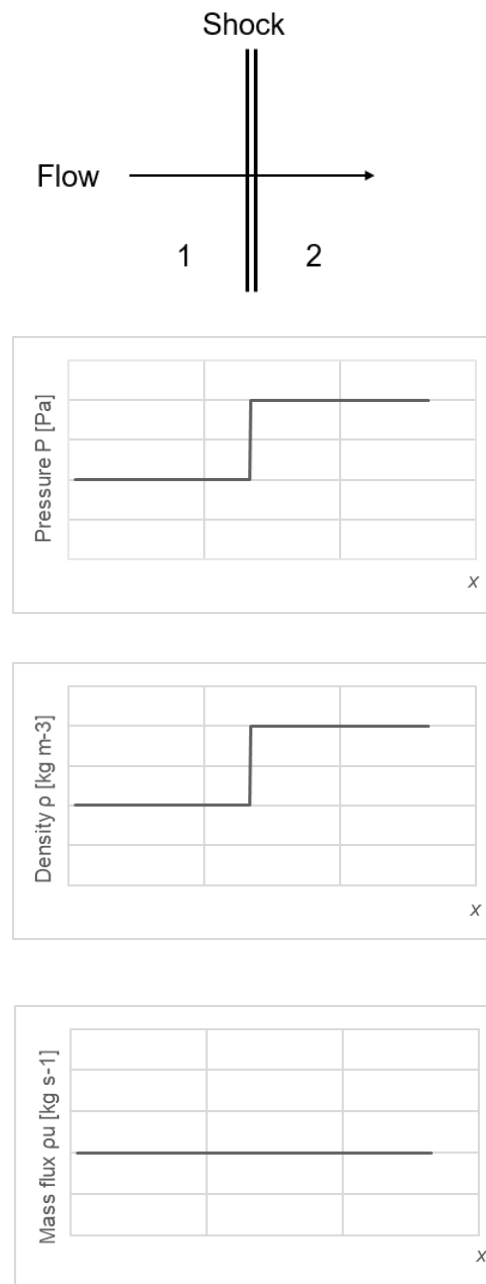


Figure 7: Variation of flow properties through a normal shock: (a) Pressure, (b) Density, and (c) Mass flux.

Shock waves develop as fluid is deflected by an object in motion, essentially decreasing the flow area and turning the fluid into itself. Depending on the geometry of the object in question, different types of shockwaves will develop. How and why each type of shock develops is beyond the scope of this research, however, the differences are of great importance. Figure 8, below, shows an example of each type.

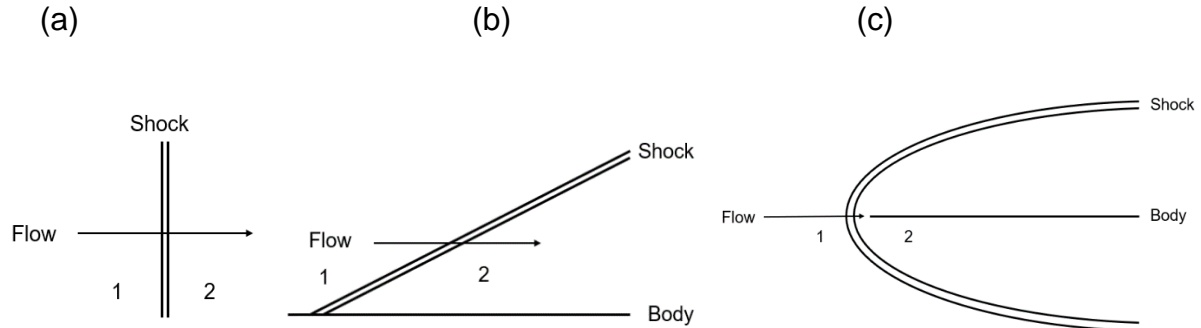


Figure 8: Types of shock wave: (a) normal, (b) oblique, (c) bow

A normal shock, Figure 8 (a), develops perpendicular to the direction of flow, commonly in supersonic inlets or over the top edge of aerofoils where it separates regions of supersonic and subsonic flow. Oblique shocks (b) however are inclined to the flow direction and often occur at the leading and trailing edges of aerofoils and blunt bodies. In turn, bow shocks (c) are a variation of oblique shocks that have detached from the leading edge (bow), due to a high angle of deflection, usually from a blunt body. Bow shocks are most well-known from renders of return capsules from various space programs or movies. Bow shocks greatly increase the drag of an object and thus are imposed purposely.

Of last concern are the heat transfer effects, which can be split into three methods of thermal energy exchange: Conduction, Convection and Radiation. But to understand in detail the heat transfer that occurs at high speeds the phenomenon of boundary layers must be well understood. As we now know, aerodynamic forces depend greatly on the local fluid properties: compressibility, velocity, density and in a complex manner the viscosity of the fluid; its 'stickiness' in a naive sense. As fluid moves past an object, the molecules closest to the wall will 'stick' to the wall creating a no-slip condition (zero velocity at the wall) (Winterwerp and Kesteren, 2004). The molecules passing over these are then in turn slowed, and so on. Figure 9 below shows a simplified velocity profile at the wall starting at the "no-slip" condition and ending in the "free-stream".

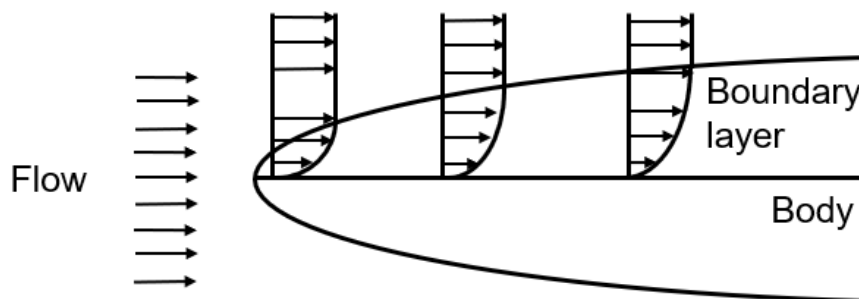


Figure 9: Boundary layer over a flat plate

The slowing of fluid from Mach 2.0 to zero at the wall causes massive heat generation, therefore, in the theory of heat transfer, a thermal boundary layer occurs. Understanding the existence of these layers at the surface of the body is essential to being able to correctly model the flow using CFD as we also must consider their interaction with shock waves.

Computational Mechanics – Theory of numerical computing

The foundations of CFD are built upon three governing equations in fluid dynamics, the energy, continuity, and momentum equations. These are mathematical representations of physical principles we confront daily; energy conservation, mass conservation and Newton's second law respectively – within CFD literature these equations can be often referred to as transport equations. As with many topics, the governing equations' derivation is beyond the framework of this paper, but J.D. Anderson offers great insight in 'Computational Fluid Dynamics, An Introduction (Anderson, 1995).

In CFD we see these physical principles applied through a Eulerian reference frame where we define control volumes (finite elements) which are fixed in space. By applying boundary conditions such as inlets, outlets, and walls we can quantify the fluid properties within each volume by applying the governing equations. With this information the solver can then iterate towards a solution providing the user with the residuals from the control volume at each timestep. These residuals are the direct imbalance in each of the governing equations from every control volume; since simulations often feature meshes with element numbers to the 3rd order the user is given the root-mean-square (RMS) of all the residuals in the domain to monitor their convergence towards zero.

This however raises several important issues:

- 1) The solution may be dependent on the mesh created by the user
- 2) A solution may never be found or take too long to find
- 3) Computational resources must be balanced with accuracy

To put these ideas into perspective, consider a numerical case of a 1D conduction in a bar, represented in Figure 10. The bar has been discretized into 3 mesh elements, 4 nodes by the user and boundary conditions have been applied.

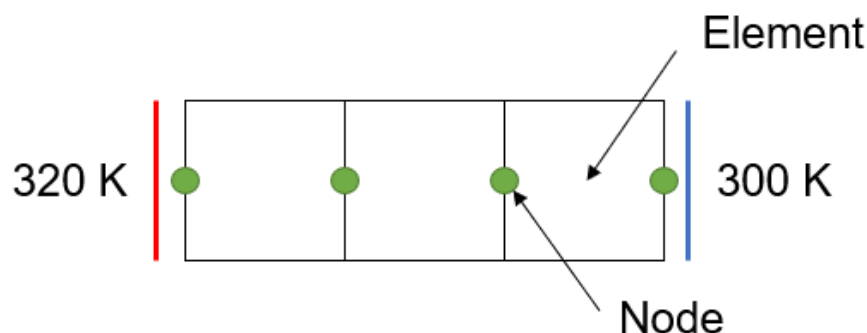


Figure 10: (a) 1D metal bar

The solver using this boundary value problem can create a system of algebraic equations for each node, relating it to its neighbours. These algebraic equations are then calculated iteratively by the solver. Figure 10 (b) shows two numerical solutions with differing numbers of elements showing the dependency of each node on the value of its neighbours.

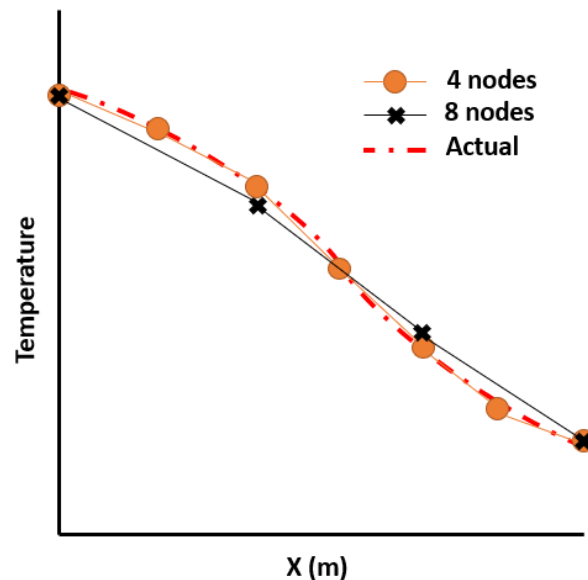


Figure 10: (b) Temperature distribution of 1D conduction

From this we can see that increasing the number of elements positively affects the outcome of the solution, however as mentioned previously, the more elements, the more algebraic equations the solver has to handle and the longer the simulation will take. Therefore, there a balance must be struck where a finer mesh is used where the solution variables have a high gradient and a coarse mesh where they change very little.

Concluding the theory of numerical computing is a topic still regarded as one of the most important mathematical questions of our time, and forms one of the Clay Institute's; Millennium prize problems, a solution to the Navier-Stokes – a numerical solution to turbulence.

Turbulence is one of two types of fluid motion, the other laminar, characterized by chaotic changes in its flow properties. It is believed, but yet to be proven, that the Navier-Stokes equations correctly describe turbulence thus making numerical solutions for turbulent flow very difficult. To counter the numerical complexity, time-averaged equations such as the Reynolds-Averaged Navier-Stokes (RANS) equations which in turn are complemented with turbulence models are applied. Flow regimes encountered such as in this study commonly use the: k-omega model, Shear-stress transport (SST) model or the Spalart-Allmaras (SA) model – their relative strengths are discussed below, Table 1.

Table 1: Comparison of common turbulence models (Hanjalić and Launder, 1972; Wilcox, 2008; Menter, 1994)

Model	K-omega (k- ω)	SST	S-A
What is it?	Commonly used, two-equation model – one equation for the turbulent kinetic energy k, and one for the specific dissipation ω .	Combines the k- ω and k-epsilon (k- ϵ) models to utilize their respective advantages. K- ω near the wall and K- ϵ (ϵ meaning dissipation of turbulent kinetic energy) in the free stream.	One-equation model commonly used for high speed aerodynamic problems which solves for turbulent viscosity transport.
Strengths	Best used for near wall flows and can resolve complex boundary layer interactions under adverse pressure.	Performs well in adverse pressure gradients and areas of flow separation.	Less computational intense due to solving only one equation. Has undergone extensive validation for external flows.
Weaknesses	Typically overpredicts flow separation at walls requiring a high mesh resolution (more computational intense).	Regions of high acceleration or stagnation fall subject to overestimations of turbulence levels, k.	Underpredicts turbulence length as well as separation and is known for numerical instability in shear flows.

A comprehensive numerical study conducted by Guillermo Araya in 2019 applies these turbulence models to a flat plate model to investigate differences in lift, drag and skin friction coefficients (shown in table 2) and validate the model against previously available experimental data for the same flow regime. Guillermo concluded that for attached or separated flows, the results vary little between the solutions, however, recirculation and local pressure coefficients stood out as more accurately determined by SST (Araya, 2019).

Table 2: Coefficient comparison for flat plate using different turbulence models (Araya, 2019)

Model	k- ω	SST	S-A	[Cook, et al. 1979]
C_l	0.801	0.811	0.792	0.803
C_d friction	0.0054	0.0054	0.0064	N/A
C_d total	0.0175	0.0178	0.0182	0.0168

Computational Mechanics – Previous literature

Flat plates are commonly investigated as a baseline study for many aerodynamic problems as they are in this one. Therefore, there are a plethora of studies surrounding their behaviour in different flow regimes. Grid fins, however, in the context of this study are yet to have computationally extensive work undergone due to their typical application in munitions; the common goal is usually to decrease drag, not increase it. Many are also limited by their discussion of setup and thus cannot be recreated.

Meshing is an important and core component of CFD which, to be successful must consider the geometry and flow it's being applied to. Unfortunately, published papers often lack comprehensive detail on their meshing techniques and structure, only including points like, “unstructured” or “triangular” (Maruyama et al., 2011; Srinivasan, Vijayan and Sridhar, 2017). Whereas details referring to mesh independency studies, non-dimensional distances for turbulence models and application of symmetry should be considered. Roy and Blottner, (2006) investigate the differences imposed on a supersonic flat plate due to the turbulence model selection and subsequently when considering the SST model mentions y^+ (describes

the height of the first element from the wall). Whilst this is an important consideration, the element size elsewhere in the domain is also important. Areas of high gradients such as shock waves require a fine mesh resolution to be properly captured, remembering, shocks are an instantaneous occurrence (200nm thick). Roy and Blottner (2006) and Akansu et al. (2008), all overlook this importance and thus omit mesh independency studies due to a limit on computational effort. Meshing should first be conducted coarsely and then progressed to a finer more resolute mesh to ensure results are independent of their mesh sizes (Wibowo, 2019; Lippert et al., 2005).

As previously laid out in Table 1, SA and SST are commonly seen throughout high-speed compressible CFD papers. Roy and Blottner (2006) argued that both SA and SST perform well in supersonic flow, correctly estimating surface heat flux and upstream pressure. And concluded their superior application for external flows through their extensive validation. Netimi and Moghimi (2014) add that despite SA being a simple one-equation model it shows acceptable performance and thus it may be less economical to use more complex models. Whilst it is important to consider the economic impact, the shortcomings of SA in areas of flow separation in some geometries are too great (Matsui et al., 2020).

Finally, Verification of CFD models before application is often omitted from grid fin research (Srinivasan, Vijayan and Sridhar, 2017; DeSpirito et al., 2000; Schülein and Guyot, 2006) when it should be an important and often large section. Verification against a baseline study proves that the solver is producing results within an allowable margin of error and those solver settings are applied accordingly, as discussed in section 4.1. Tekure (2021) investigates the effect of Mach number and plate thickness on the heat transfer effects of a flat plate in supersonic flow. Suitable validation cases must extensively report the set-up of their solver, including boundary conditions, initialisation, solver, and output controls and how the fundamental equations are applied to the solution. For that, Veeresh Tekure's "Effect of Mach number and plate thickness on the flow field and heat transfer characteristics of supersonic turbulent flow over a flat plate at different thermal boundary conditions", from the *European Journal of Mechanics* will be used as Verification. Figure 13, below, summarises domain from Tekure's case.

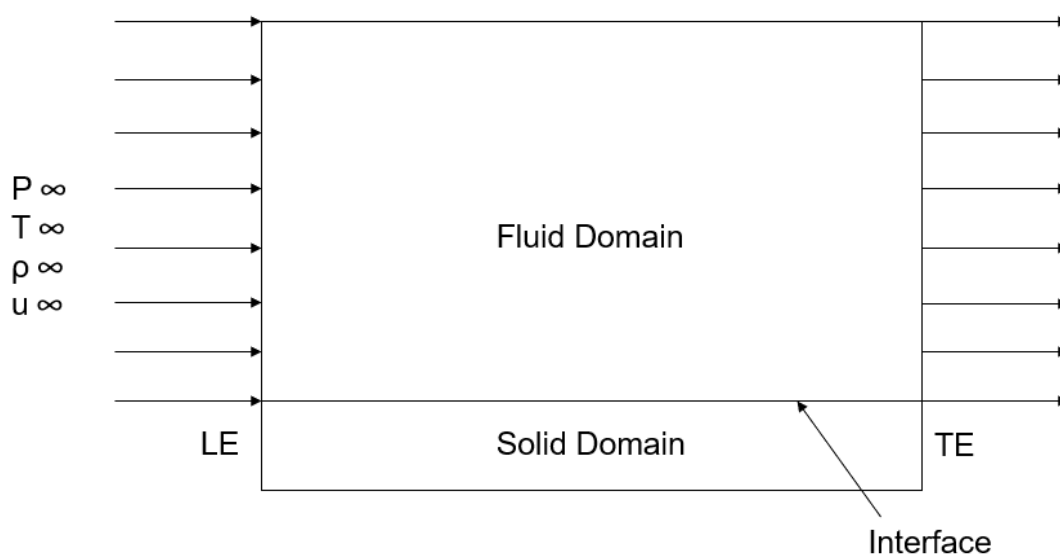


Figure 1: Schematic of the computational domain from Tekure (2021)

Code Comparison

Commercially available CFD codes ANSYS-CFX and ANSYS-Fluent, despite both being owned by ANSYS, were developed separately, and discretise the Navier-Stokes (NS) equations differently affecting results. ANSYS-CFX uses a vertex-centred scheme in which the flow variables are stored at the grid point and the control volume is defined by the cells sharing the grid point (Fig. 14 (a)). ANSYS-Fluent however, uses a cell-centred scheme which stores the flow variables at the centre of the cell and variables are defined by the fluxes of adjacent cells, (b). To assess the impact of this difference, an oblique shock was modelled over a ramp at Mach 2.5 in air per Frank White's "Fluid Mechanics" (White, 2009).

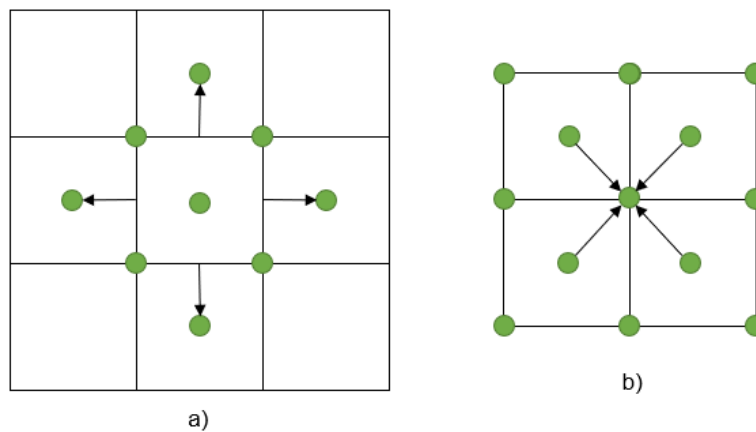


Figure 14: Control volumes of (a) vertex-centred scheme, and (b) cell-centred scheme

Method

The 2D model is a reproduction of an example solution from Frank White's "Fluid Mechanics" (White, 2009) in ANSYS-CFX and -Fluent. The example models a body with a 15-degree ramp where the oblique shock is introduced (represented by the black-dashed line Figure 15). The computational domain extends 1 metre upstream from the turning point and 1 metre parallel to the ramp. The domain is discretised using a fully tetrahedral mesh using ANSYS-CFX AND ANSYS-Fluent.

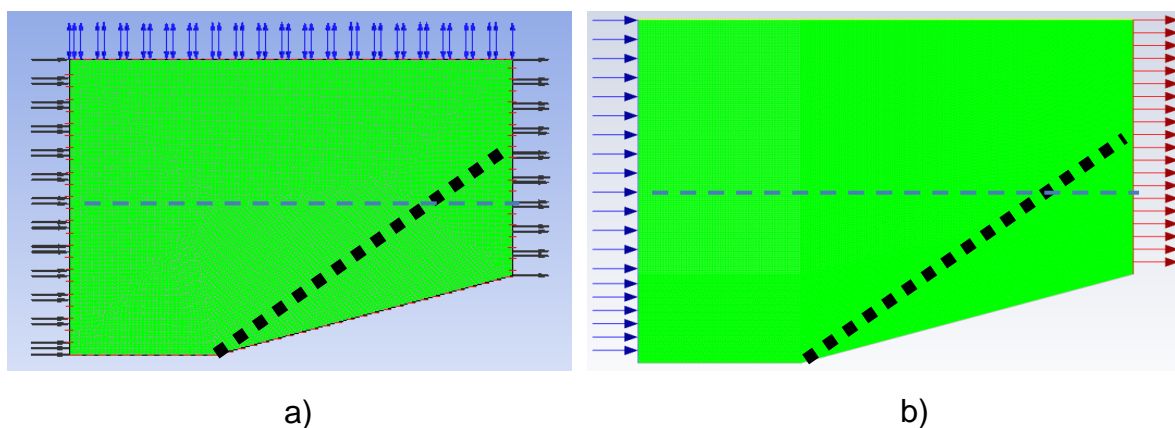


Figure 15: Discretised domain in: (a) ANSYS-CFX, (b) ANSYS-Fluent

Modelling Assumptions

1. Ramp is modelled as two-dimensional with symmetry applied on all walls in YZ thus, it is assumed the ramp has an infinite span.
2. The walls are modelled as isentropic, and thus the air transfers no heat to the body surface.
3. It is assumed that the shock angle is identical in both studies.
4. It is assumed that simulation validity is already achieved as provided by the ANSYS fluids verification manual.

Setup

The assumed boundary and domain conditions are detailed in Table 3 below. In this method, ANSYS-CFX-R2 and ANSYS-Fluent are used separately in two cases to solve the discretised RANS equations. All cases are steady-state and utilise a variable timescale to achieve a residual convergence of 1 E-06.

Table 3: Problem specification

	Details	Option/Value	Units
Boundaries			
Inlet	Flow Regime	Supersonic	n/a
	Velocity	852.68	m/s
	Temperature	289	K
	Static Pressure	-74274.9	Pa
Outlet	Flow Regime	Supersonic	n/a
Ramp	Mass/Mom.	No-Slip	n/a
	Heat transfer	Adiabatic	n/a
Domains			
Fluid	Material	Air (Ideal)	n/a
	Heat Transfer	Total Energy	n/a
	Turbulence Model	None (Laminar)	n/a
	Temperature	289	K

Results

Carried out utilising a verification manual (ANSYS, 2021) and Fluid Mechanics (White, 2009), an oblique shock was modelled over an inclined ramp. Along the centreline of the domain, the Mach number and Temperature were plotted against the x-wise position (reflected by the blue line in Figure 15 (a) and (b)). Figures 16 and 17 below show the variation between the two solvers for two flow variables.

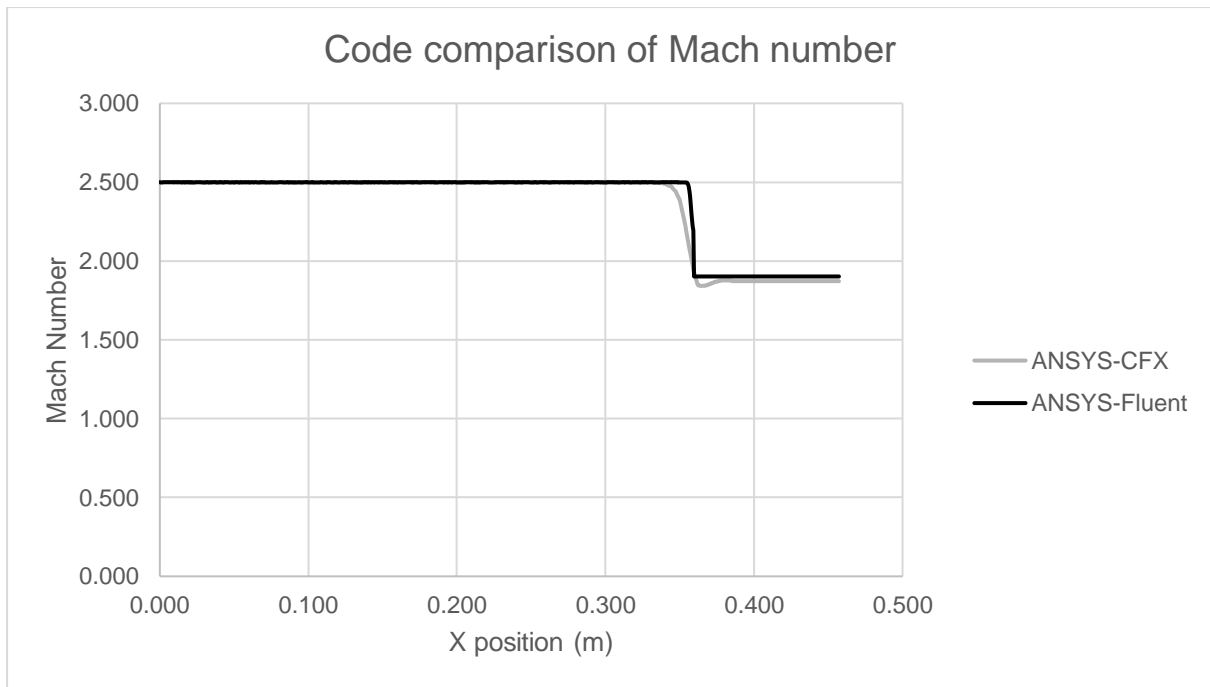


Figure 2: Mach number in CFX and Fluent against x-position

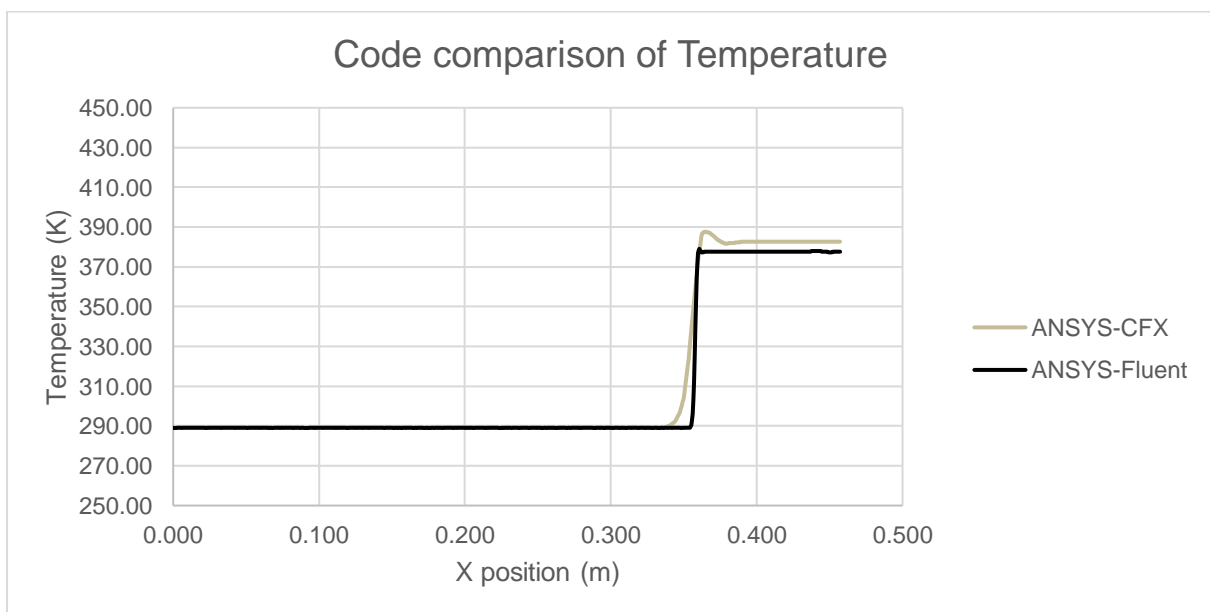


Figure 3: Temperature in CFX and Fluent against x-position

To visualise the temperature variation seen in Figure 17, see the temperature contours below in Figure 18, a) and b).

Using the derivations from Appendix B as seen in Section 4.1.4, the codes can be compared to analytical calculations.

Table 1: Ratio of variables in CFX and Fluent to analytical values

		ANSYS-CFX		ANSYS-Fluent	
Variable	Target	Actual	Ratio	Actual	Ratio
Mach Number	1.874	1.871	0.9984	1.902	1.015
Temperature, K	382.0	382.8	1.002	377.6	0.9885
Density, kg/m ³	2.277	2.278	1.000	2.233	0.9807

Target values in Table 4 are provided by solutions in “Fluid Mechanics” (White, 2009).

Discussion

Both ANSYS solvers give an accurate insight into the shockwave behaviour in this case. Considering the coarse meshes used in these cases the results shown in Figure 17 align with the step functions discussed earlier. However, because of this coarse mesh, the Temperature and Mach Number change at the shockwave does not appear to be an instantaneous, discontinuous change in the fluid properties so neither solution are entirely mesh independent.

However, the main difference between the two codes was the time to converge. ANSYS-CFX took ~450 iterations, approximately 1 hr, to reach a reliable convergence ($1.0E-06$) whereas ANSYS-Fluent took ~4000 iterations to converge, 3hrs. Whilst ANSYS-Fluent completed each iteration quicker, it took sizably longer to converge. This can be accredited to ANSYS-CFX’s coupled solver that creates a global matrix to simultaneously solve for all variables for its system of algebraic equations. Unlike ANSYS-Fluent which solves for variables sequentially (Johnson, 2015).

Analysing the flow variables against position (Fig. 16 and 17) ANSYS-Fluent better predicts the shock thickness as seen by the steeper gradient. Whereas ANSYS-CFX predicts the variable discontinuity over a larger distance. This suggests that ANSYS-CFX requires finer mesh resolution in areas of high gradients than ANSYS-Fluent.

Considering the limited numerical difference between the two solvers but the additional computational requirements of ANSYS-Fluent, ANSYS-CFX is the more efficient and will be subsequently used for the remaining studies.

Key Observations

1. CFX requires a finer mesh resolution in regions of high gradients, increasing computational effort.
2. Fluent, due to its solver, takes 3x as long to reach reliable convergence compared to CFX.
3. Fluent overpredicts the flow variables across the shock by an average percentage error of 1.52% whilst CFX, is 0.14%.

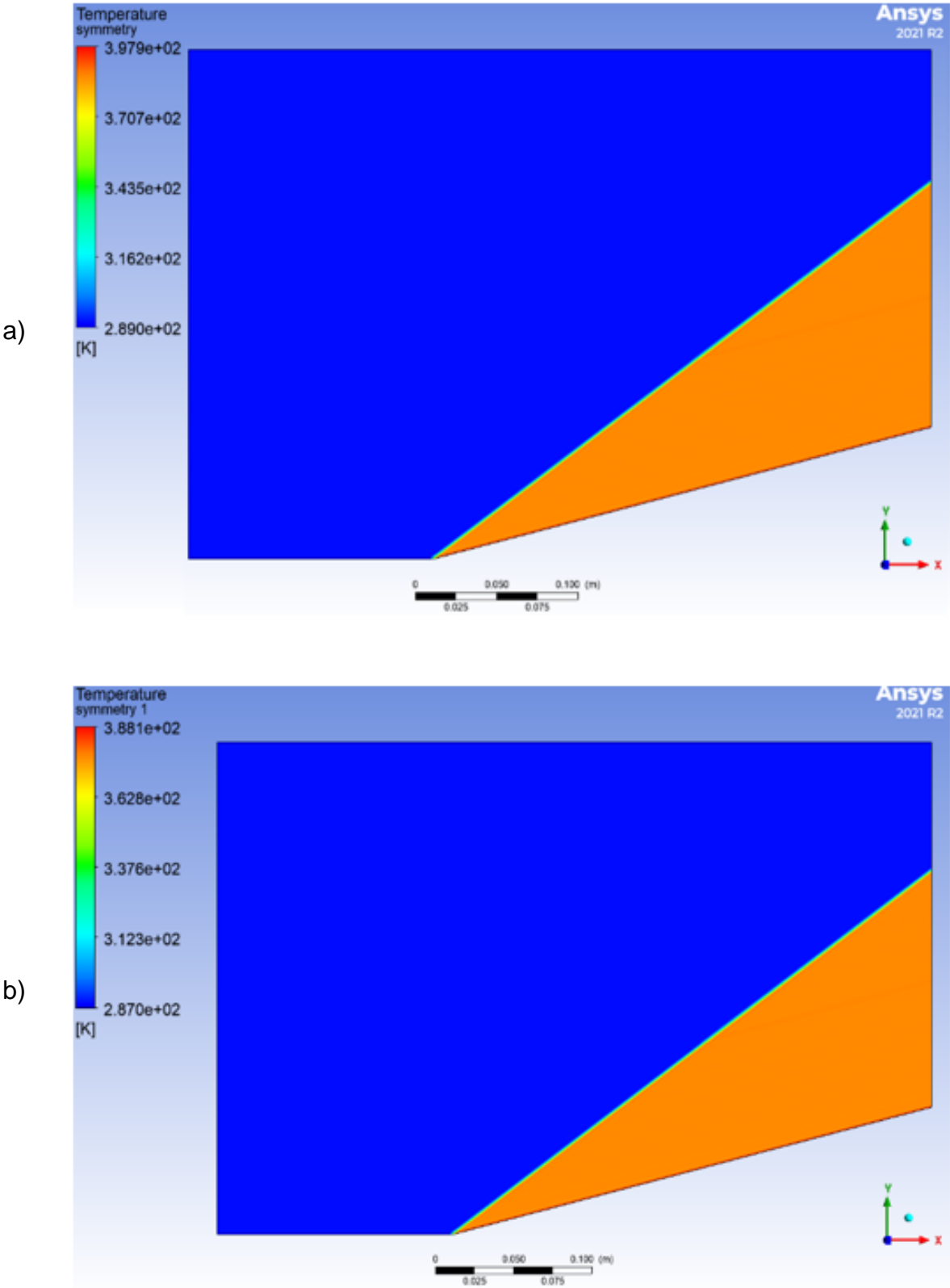


Figure 4: Temperature contour: (a) ANSYS-CFX, (b) ANSYS-Fluent

2-dimensional flat plate

Method

This chapter aims to demonstrate the accuracy of the ANSYS-CFX code on baseline geometry by comparing it to a previously validated CFD model so that it may be applied to more complex geometry with confidence. The study is a comparison of computational results between this work and that detailed in section 2.3 (Tekure, 2021). It details a study of a 2D flat plate travelling at Mach 2.0 in air; investigating the heat transfer effects between the solid (aluminium 6060-T6) and fluid (air, ideal gas) domains. The wall pressure and normalised temperature were measured across the domain and sampled at various locations to compare with this work.

Geometry and Meshing

The 2D model was reproduced in ANSYS-SpaceClaim from existing literature, Tekure (2021). The model is a 2mm thick, 50mm long flat plate at 0° angle of attack (AoA). The computational domain extends $\frac{1}{4}$ the plate length upstream, 1.5 above and 2.5 plate lengths downstream of the plate. A fully hexahedral mesh was generated using ANSYS-SpaceClaim Meshing Tool (Fig. 19).

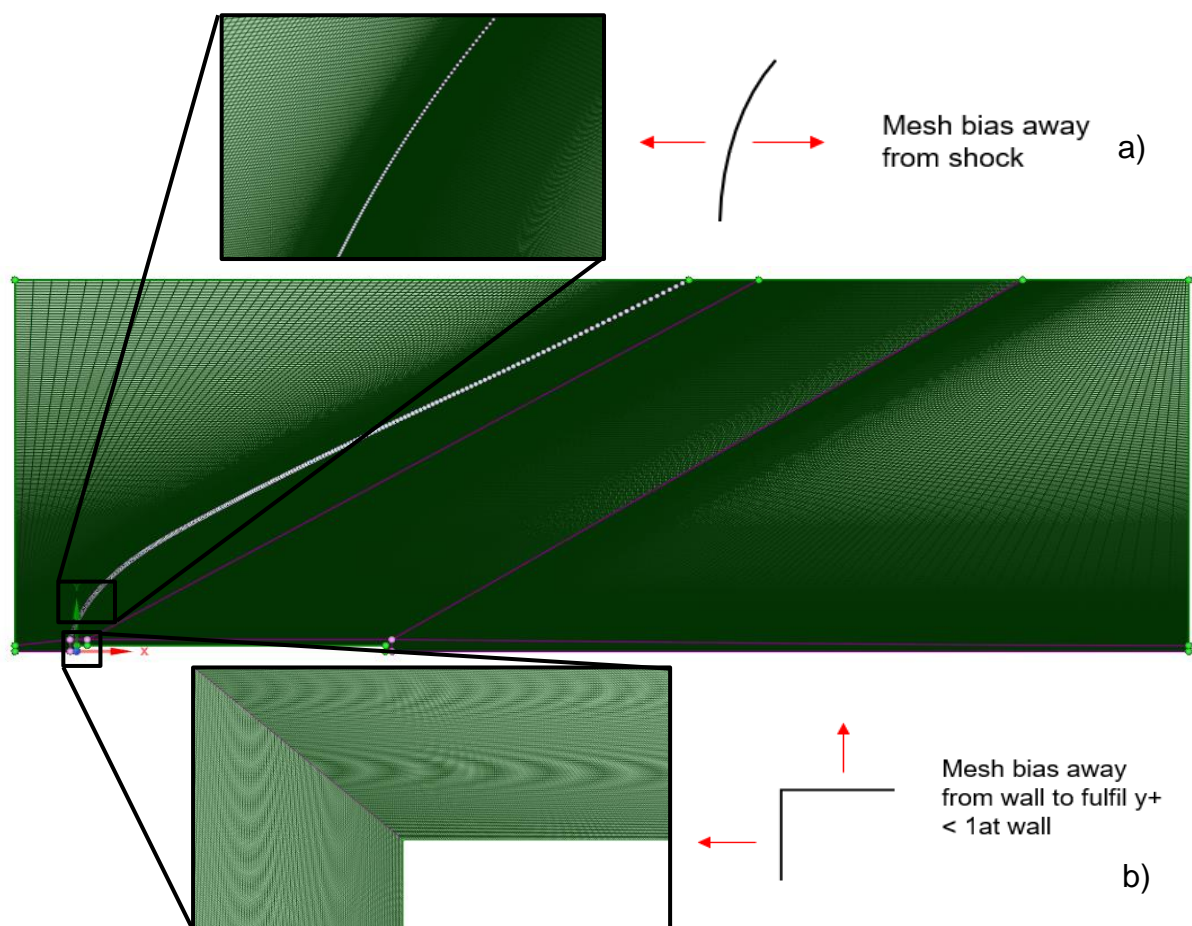


Figure 5: Hexahedral mesh in the domain with highlighted areas of interest: (a) Mesh at the shockwave, (b) Mesh in the boundary layer region

Discretization of the domain followed best practice guidelines by Menter et al. (2015) and ANSYS (2021) for the Shear Stress Transport turbulence model.

Modelling Assumptions

1. The plate is assumed to be perfectly aligned with the oncoming flow and thus the flow field is symmetrical about the plate's neutral axis.
2. Surface roughness of the plate material is neglected and is thus modelled as a smooth surface.

Setup

The assumed boundary and domain conditions are detailed in tables 5 and 6 below. In this method ANSYS-CFX-R2 is used to solve the discretised RANS equations. In all cases steady-state solutions are conducted utilising a variable physical timestep to achieve a residual convergence of 1 E-06. Domain temperatures are specified for initialisation only.

Table 2: Baseline case boundary conditions

Boundary	Details	Option/Value	Units
Inlet	Flow Regime	Supersonic	n/a
	Velocity	686	m/s
	Temperature	169.44	K
	Static Pressure	17500	Pa
	Turbulence Intensity	5	%
Outlet	Flow Regime	Supersonic	n/a
Plate	Mass/Mom.	No Slip	n/a
	Roughness	Smooth	n/a
Domain walls	Mass/Mom.	Free Slip	n/a
	Heat transfer	Adiabatic	n/a

Table 3: Baseline case domain conditions

Domain	Details	Option/Value	Units
Fluid	Material	Air (Ideal)	n/a
	Heat Transfer	Total Energy	n/a
	Turbulence Model	SST	n/a
	Temperature	169.44	K
Solid	Material	Aluminium	n/a
	Heat Transfer	Thermal Energy	n/a
	Temperature (t=0*)	322.22	K

* $t=0$ relates to the initialisation conditions of the solver.

Simulation Validity Study

A complete mesh independency study was conducted on a baseline domain extending 1 plate length upstream, 6 above the plate, and 10 plate lengths downstream to ensure that results were independent of mesh resolution. Table 7 shows the associated simulation results to mesh resolution in the fluid domain and is represented graphically in Figure 20.

Table 4: Baseline case fluid domain mesh study

Simulation no.	Total elements	Elements at plate	Total drag (N)	Leading edge (LE) Pressure (Pa)
1	215000	54000	9.589	42361
2	415000	82000	8.1	41532
3	510000	111000	8.56	36531
4	780000	166000	10.35	29132
5	1120000	283000	11.4	26780
6	1500000	376000	11.67	23357
7	1650000	412000	11.71	23127
8	1800000	450000	11.72	23026
9	2150000	537000	11.72	22961

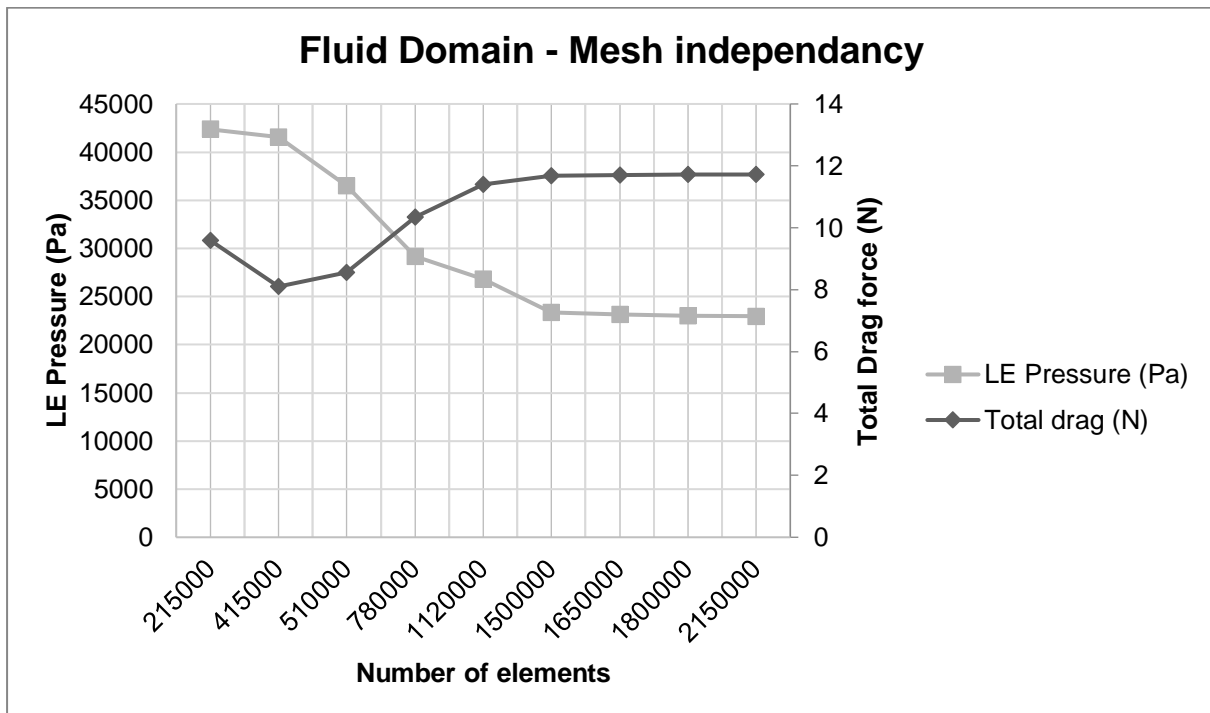


Figure 6: Baseline case fluid domain mesh study

Using the 1.5 million mesh-independent solution, the effect of mesh resolution in the solid domain was investigated.

The normalised temperature is found by the ratio of local temperature to the free stream, shown in equation 1:

$$\vec{T} = \frac{\bar{T}}{T_{\infty}} (1)$$

Table 5: Baseline case solid domain mesh study

Simulation no.	Total elements	Normalised Temperature at LE	Normalised Temperature at Trailing edge (TE)
10	500	1.7	1.5
11	2000	1.578	1.71
12	8000	1.66	1.77
13	23000	1.7	1.81
14	128000	1.698	1.82
15	512000	1.695	1.82

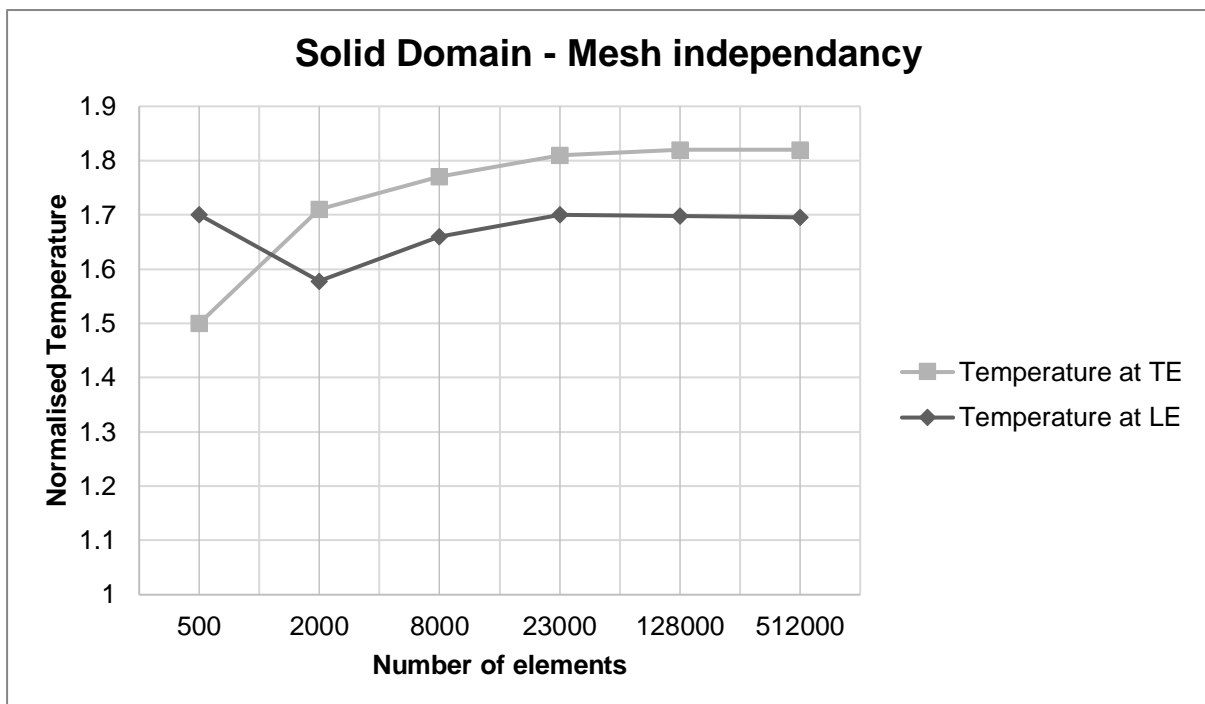


Figure 7: Baseline case solid domain mesh study

It is important to consider the conjugate nature of variables within a simulation; measurement of just Mach number throughout the domain would suggest that mesh independency is reached at 1.12 million elements. However, this would lead to a measured 2.30% underprediction in total drag.

Therefore, all subsequent results for this simulation are obtained using a mesh of 1.5 million elements in the fluid domain and 23,000 in the solid.

For optimal performance of Menter's SST model, the boundary layer requires sufficient resolution. The main criterion to judge this is the minimum spacing between boundary layer nodes and the wall.

A target value of $y^+ = 1$ for the SST model. The actual distance between the first node and the wall is defined by the characteristic length Reynolds number (Eq. 3).

$$\Delta y = C_l(y^+)\sqrt{74}Re_L^{-13/14} \quad (2)$$

Table 6: Calculation of minimum wall-to-node distance

Property	Value	Units	Formula
Reynolds Number	1.86E+06	N/A	$Re_L = \frac{\rho u C_l}{\mu}$ (3)
Chord length	0.05	m	
Δy	6.48E-07	m	Equation 2

Therefore, to fulfil a y^+ of 1, the first node height must be at 6.48E-07m above the plate. This is unreasonable for the entire span of the plate; therefore, bias factors are applied (Fig. 19) to reduce computational effort.

In addition to mesh independency studies, the effect of domain sizing was also investigated. The baseline domain was first halved and then quartered in all directions. Table 10 lists the corresponding simulation results.

Table 7: Baseline case domain sizing study

Variable	Baseline domain	Halved domain	Quartered domain
Total drag (N)	11.67	11.67	11.68
Normalised LE Temperature	1.698	1.698	1.698
LE Pressure (Pa)	23357	23363	23378

The domain study shows that the solution appears to be insensitive to domain size variation. The largest to smallest domain sizes saw a 0.09% difference in total drag and no measurable difference in maximum plate temperature. Therefore, the quartered domain is used for the rest of this study to reduce computational effort with minimal to no expense on result validity.

Results

The 2-dimensional flat plate study was compared with Tekure's research on flat plate heat transfer (2020) as previously described. Figure 22, below, shows the wall pressure P_w , across the top of the flat 50mm plate.

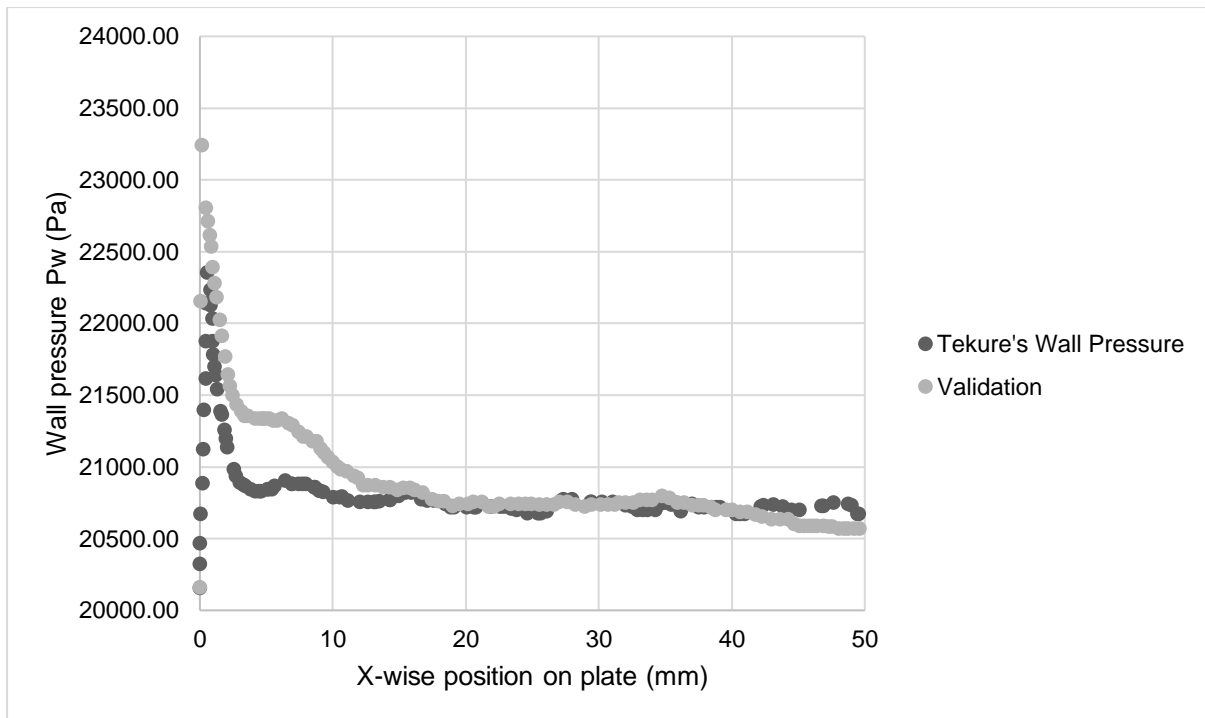


Figure 8: Wall pressure comparison of numerical study and Tekure's literature

The wall pressure largely shows good agreement with Tekure's study, the pressure at the leading edge of the plate has the greatest deviation of 3.79%. Moving aft however the pressure is in better agreement.

The profiles of temperature variation shown in Figure 23 (a) and (b) are in good agreement when accounting for the bow shock in (b).

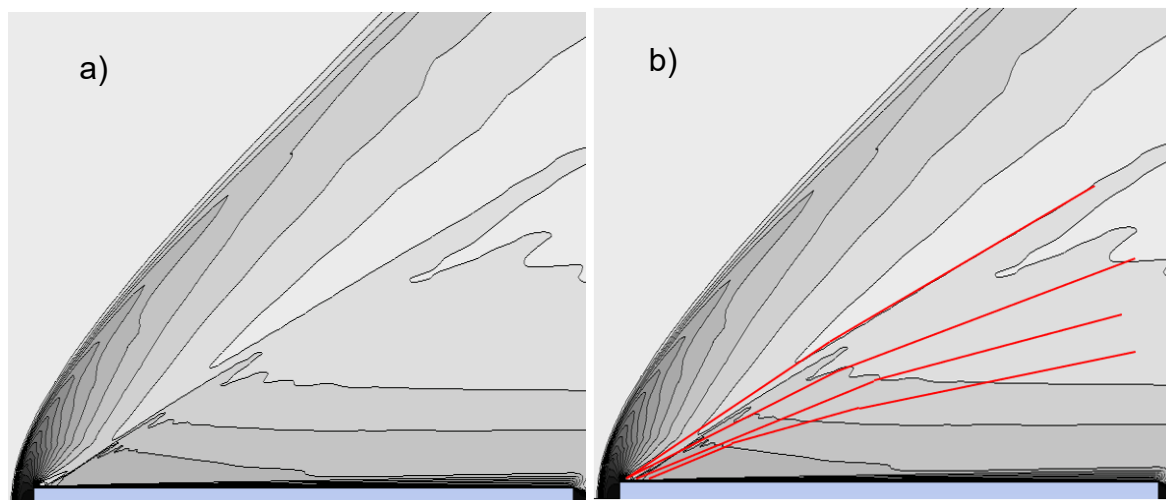


Figure 9: Temperature profiles: (a) Simulation results, (b) Tekure simulation overlayed

Normalised (with the free stream) temperature plots (Fig. 24 and 25) show the variation temperature across two vertical lines. Each data point represents an intersection between the line and a temperature contour.

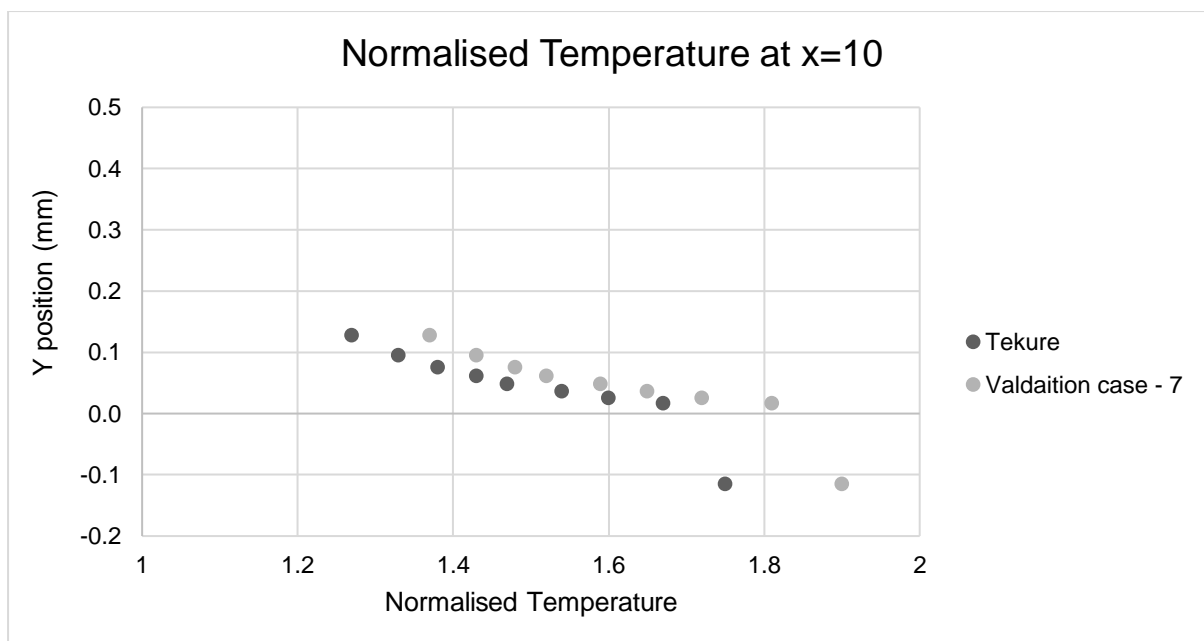


Figure 10: Normalised temperature at x=10 of literature and numerical study

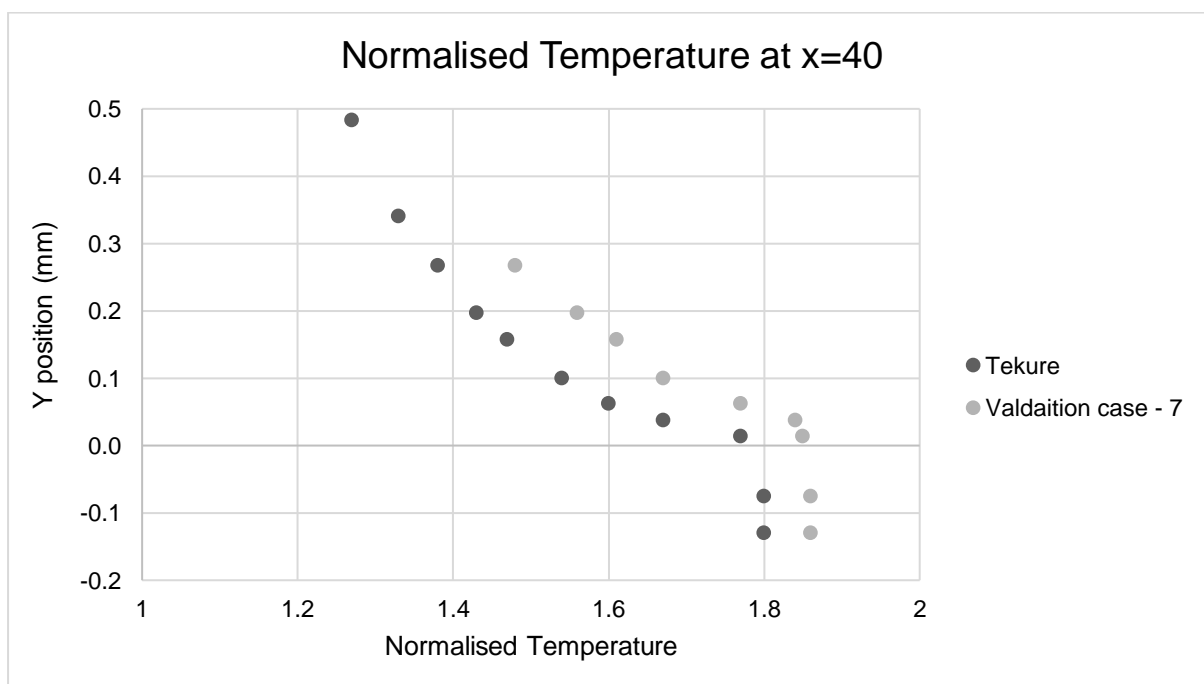


Figure 11: Normalised temperature at x=40 of literature and numerical study

To further validate the solution to Tekure's case, analytical calculations of free stream variables were completed to triangulate the results. These of course are idealisations of the true conditions.

Flow variables upstream and downstream of the shock for both cases can be derived through the application of the steady, viscous compressible Navier-Stokes equations for mass, momentum, and energy conservation.

$$M_1 = \sqrt{\frac{(\gamma-1)M_0^2 \sin^2(s)+2}{2\gamma M_0^2 \sin^2(s)-(\gamma-1)}} \frac{1}{\sin^2(s-a)} \quad (4)$$

$$T_1 = \left(\frac{[2\gamma M_0^2 \sin^2(s)-(\gamma-1)][(\gamma-1)M_0^2 \sin^2(s)+2]}{(\gamma+1)^2 M_0^2 \sin^2(s)} \right) T_0 \quad (5)$$

$$p_1 = \left(\frac{2\gamma M_0^2 \sin^2(s)-(\gamma-1)}{(\gamma+1)} \right) p_0 \quad (6)$$

Table 8: Calculation of computational errors in the baseline case

Property	Symbol	Units	Value	Formula
Ratio of specific heats	γ	N/A	1.4	Input
Upstream Mach Number	M_0	N/A	2	
Shock Angle	s	°	45	From CFX solution
Deflection Angle	a	°	5	
Upstream Temperature	T_0	K	169.44	Input
Upstream Pressure	P_0	Pa	175000	
Downstream Mach Number	M_1	N/A	1.14	Equation 4
Downstream Temperature	T_1	K	274.81	Equation 5
Downstream Pressure	P_1	Pa	72179	Equation 6
CFX Downstream Mach number	M_1	N/A	1.139	
CFX Downstream Temperature	T_1	K	271.104	
CFX Downstream Pressure	P_1	Pa	66723	
Mach Number Error		%	0.087	$\frac{\text{Observed}-\text{Expected}}{\text{Expected}} \times 100 \quad (7)$
Temperature Error		%	1.35	
Pressure Error		%	7.59	

The Mach number and temperature calculations provide similar errors to those seen in the evaluation of CFX in *Code comparison – Results*.

Discussion

The flat plate study showed good agreement with Tekure (2020) literature. However, the fundamental difference between the bow shock and oblique shock development seen in Figure 23, is responsible for differences in the solution.

Figure 24 shows a large deviation in normalised temperature in this study's validation compared to the literature. This difference is due to an area of stagnation on the top of the plate developing closer to the leading edge. This area of stagnation causes fluid that flows through it to deaccelerate to Mach 0.05 causing immense heating. Figure 26 shows the stagnation region of the present simulation. Whereas in Tekure's case the stagnation region begins at 15mm from the leading edge with only a very small 1mm thick stagnation region occurring at 10mm.

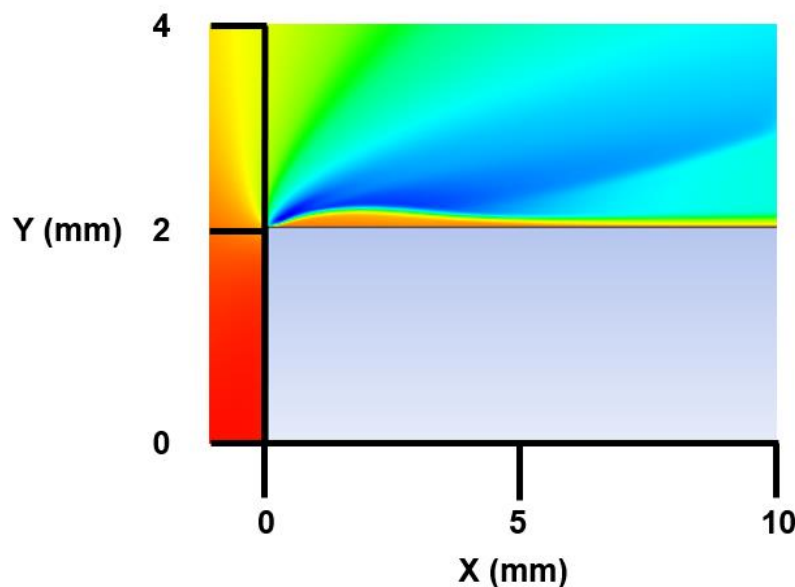


Figure 12: Comparison of stagnation region in: (a) CFD solution, (b) literature

Therefore, the magnitude of the heating doesn't vary between the two studies however, the position in which that heating occurs varies due to the development of two different shock types and their subsequent interactions with the plates boundary layer. This interaction explains the difference in leading edge temperature in Figure 24. However, the trailing edge temperature (Fig. 25) shows better agreement with the literature but differs for the same reason as the leading edge analysis. As the location of maximum temperature in the plates varies, the loosely linear decrease in temperature towards the trailing edge means that at the measured section $x=40$ mm,

The numerical solution gave a normalised plate temperature of 1.86 or 315.15K compared to 1.8 or 304.99K in Tekure's (2020) case; giving a percentage error of 3.33%.

Finally, the pressure distribution across the plate wall and the computational domain is mostly consistent with data from Tekure's (2020) literature. The peak wall pressure at $x=0$ shows a 3.98% error between datasets whereas downstream towards the trailing edge the average percentage error is 0.69%.

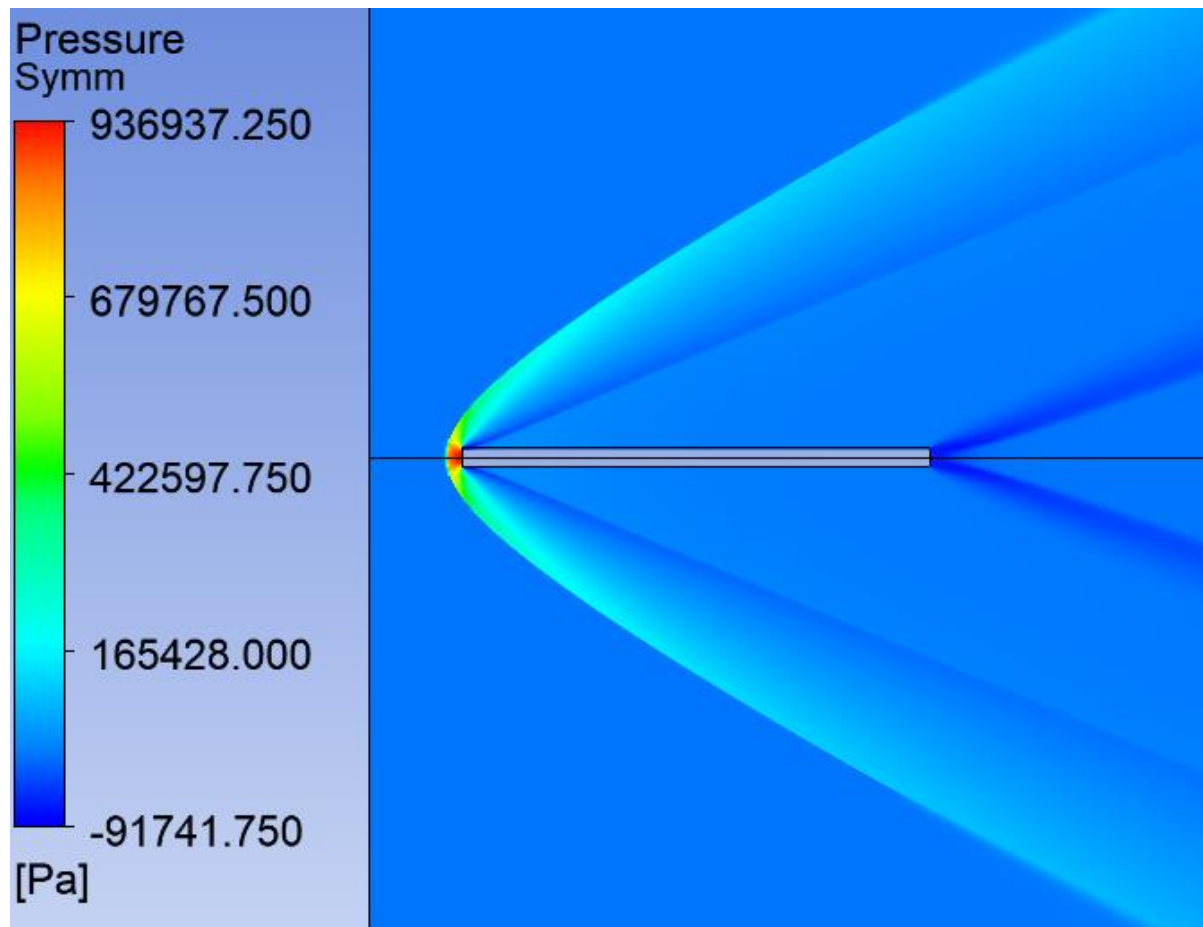


Figure 13: Pressure rendering of the baseline case

The mesh independency study (Fig. 20) whilst correct, is slightly misleading. The peak pressure itself is not decreasing. However, the location of peak pressure is moving further towards the tip of the leading edge as mesh size decreases. This is a result of the large adverse pressure gradient as fluid is turned by the plate corner. As mentioned in *Fluid Mechanics – theory of supersonic, compressible flow*, shocks are an instantaneous discontinuity around 200nm thick so to make this solution truly mesh-independent would be far too computational taxing.

Key Observations

1. Peak plate temperature occurs at different locations determined by stagnation regions on the plate surface, accurate boundary layer modelling is essential to results.
2. Drag measurement is very sensitive to LE mesh resolution.
3. First element height target of 6.48E-07m for the study Reynolds number.

2-dimensional lattice study

Once the 2D flat plate was verified, work was undertaken to investigate the shock interaction of two parallel flat plates whose dimensions are taken from Falcon 9 grid fin (Fig. 28). The conditions applied to this study are assumed to be that of the operational conditions at a single point in re-entry. The temperature distribution over the plates and the total drag was measured whilst the plate separation and thickness were varied. This aimed to identify the effects of these design features before being applied to a 3-dimensional study.

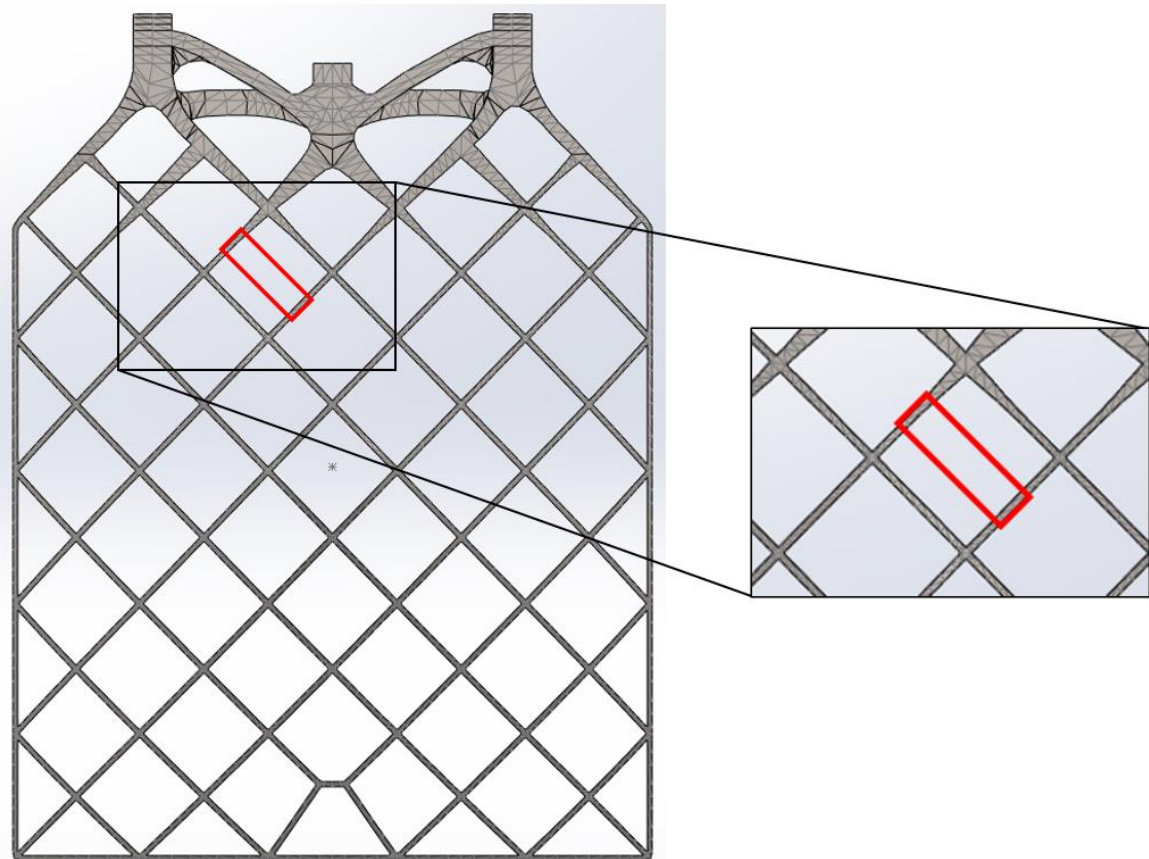


Figure 14: Lattice study geometry in the context of grid fin

Method

Geometry and Meshing

The model in this study is a 2D simplification of grid fin geometry, essentially two flat plates arranged in parallel to form a lattice. The red highlighted section in Figure 28 gives context to the geometrical origin and it can be seen in ANSYS-SpaceClaim in Figure 29. The baseline model features two 9mm thick, 168mm long flat plates with a separation of 168mm. The computational domain utilises section 3.1.4's domain independence study. Thus, the domain extends $\frac{1}{4}$ the plate length upstream, and 2.5 downstream. The domain is subsequently discretized using the ANSYS-SpaceClaim Meshing tool into a fully hexahedral mesh.

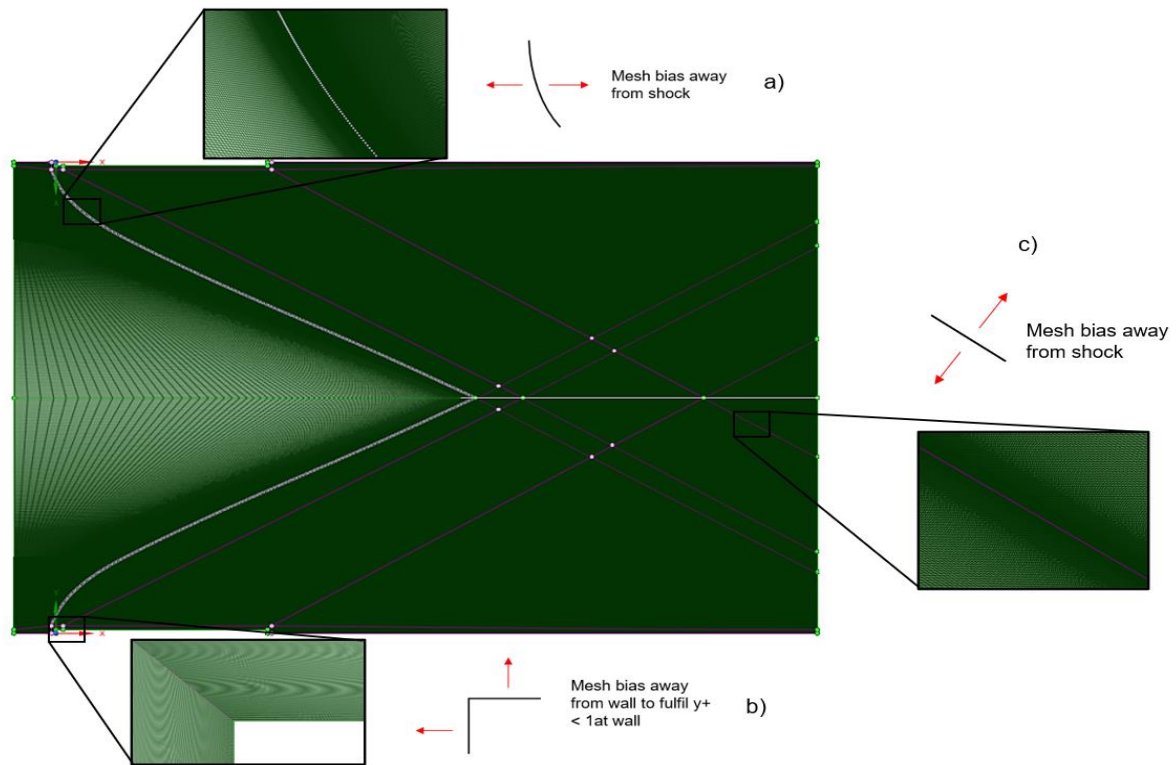


Figure 15: Simulation mesh(a) Mesh at the shockwave, (b) Mesh in the boundary layer region, (c) Mesh at downstream oblique shockwave

Modelling Assumptions

All previously made assumptions from section 3.1.2 still apply, this list features additional assumptions.

1. It is assumed that the LE and TE of each fin has identical geometry and thus chord length is constant. Figure 30 below shows the variation of the plate geometry across the back and side of the fin.
2. Inlet conditions are assumed to be constant whereas real fin velocity/temperature/pressure varies with time.
3. The fins are assumed to be perfectly aligned with the oncoming flow and hence angled at 0 degrees AoA.

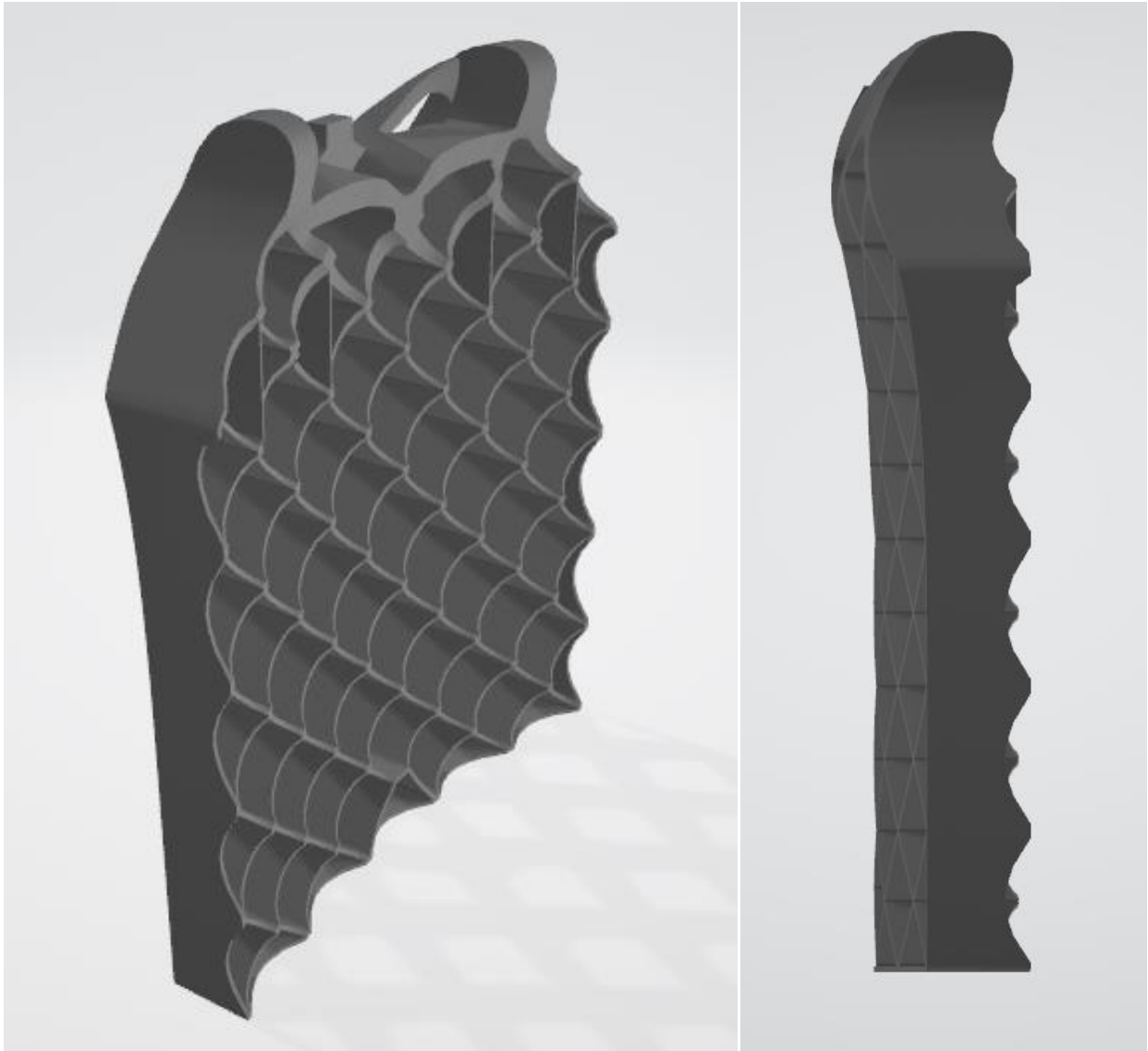


Figure 16: Variation of grid fin geometry across back and side

Setup

The assumed boundary and domain conditions are detailed below in tables 12 and 13. In this study, ANSYS-CFX-R2 is selected to solve the discretised RANS equations. The solution is assumed to be steady-state and conducted using a variable physical timestep to achieve a residual convergence. Domain temperatures are specified for initialisation only.

Table 9: Lattice case boundary conditions

Boundary	Details	Option/Value	Units
Inlet	Flow Regime	Supersonic	n/a
	Velocity	668	m/s
	Temperature	293.15	K
	Static Pressure	5470	Pa
	Turbulence Intensity	5	%
Outlet	Flow Regime	Supersonic	n/a
Plate	Mass/Mom.	No Slip	n/a
	Roughness	Smooth	n/a
Domain walls	Mass/Mom.	Free Slip	n/a
	Heat transfer	Adiabatic	n/a

Table 10: Lattice case domain conditions

Domain	Details	Option/Value	Units
Fluid	Material	Air (Ideal)	n/a
	Heat Transfer	Total Energy	n/a
	Turbulence Model	SST	n/a
	Temperature	293.15	K
Solid	Material	Aluminium	n/a
	Heat Transfer	Thermal Energy	n/a
	Temperature	322.22 (t=0)	K

To ensure numerical stability, the solver starts at a timestep of 1.5E-06 however every 250 iterations, to increase convergence, the timestep is increased by an order of 10 until a reliable convergence is achieved.

Simulation Validity Study

As with section 3.1.4, a full mesh sensitivity study was conducted, however, given the insensitivity of the solution to domain size a baseline domain was not used for this study.

Table 11: Lattice case mesh study

Simulation	Total elements	Elements at plate	Total drag (N)	LE Pressure (Pa)
1	354000	127000	1122	42361
2	548000	181000	1254.6	41532
3	1132000	365000	1167.7	36531
4	1720000	668000	1135.6	29132
5	2030000	727000	1135.46	26780
6	2740000	1290000	1135.45	23357
7	3180000	1360000	1135.45	23127
8	3540000	1510000	1135.46	23026
9	3980000	1790000	1135.46	22961

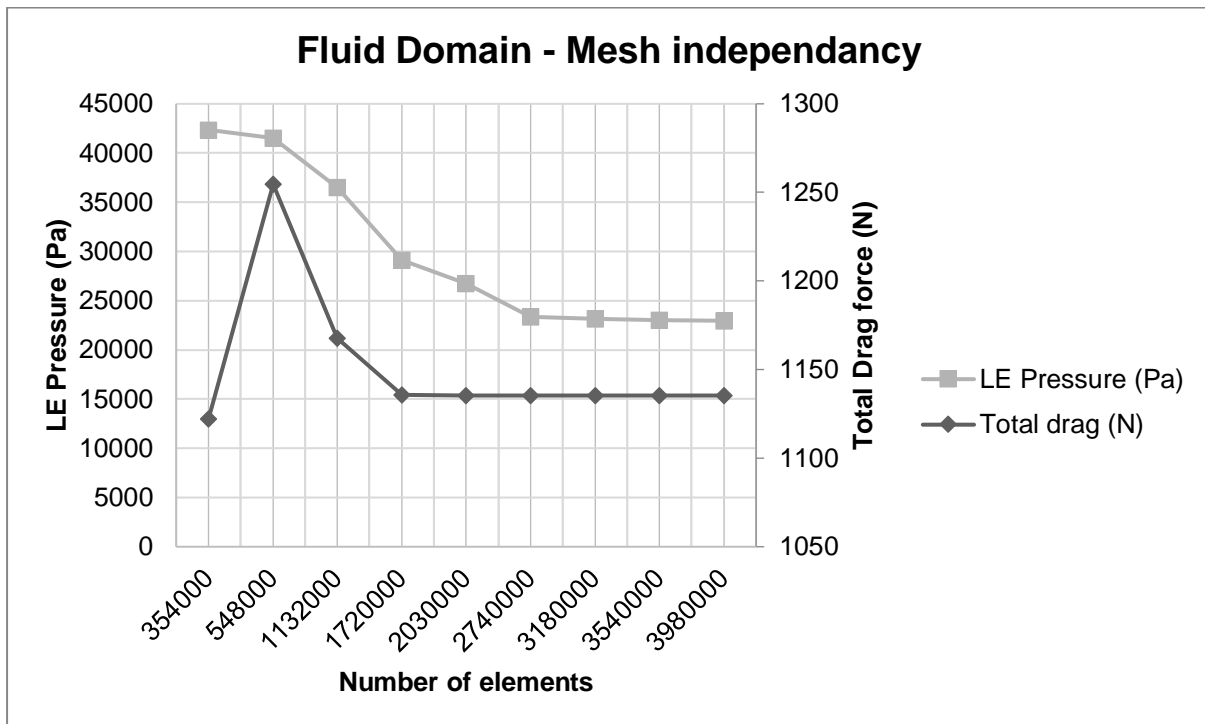


Figure 17: Lattice case fluid domain mesh study

When conducting mesh sensitivity studies, it is important to not just consider the basic output functions of the solver. Looking at total drag alone would suggest a mesh of 1.7 million elements is adequate however, the peak pressure is not correctly resolved until 3.18 million elements.

Utilizing the mesh-independent solution of 3.18 million elements the solid domain mesh was investigated for sensitivity factors.

Table 12: Lattice case solid domain mesh study

Simulation no.	Total elements	Temperature at LE (K)	Temperature at TE (K)
10	1000	411.5	415
11	4000	406.3	412
12	16000	404.6	408
13	46000	401.8	407
14	256000	402.3	407.2
15	1020000	402.3	407.3

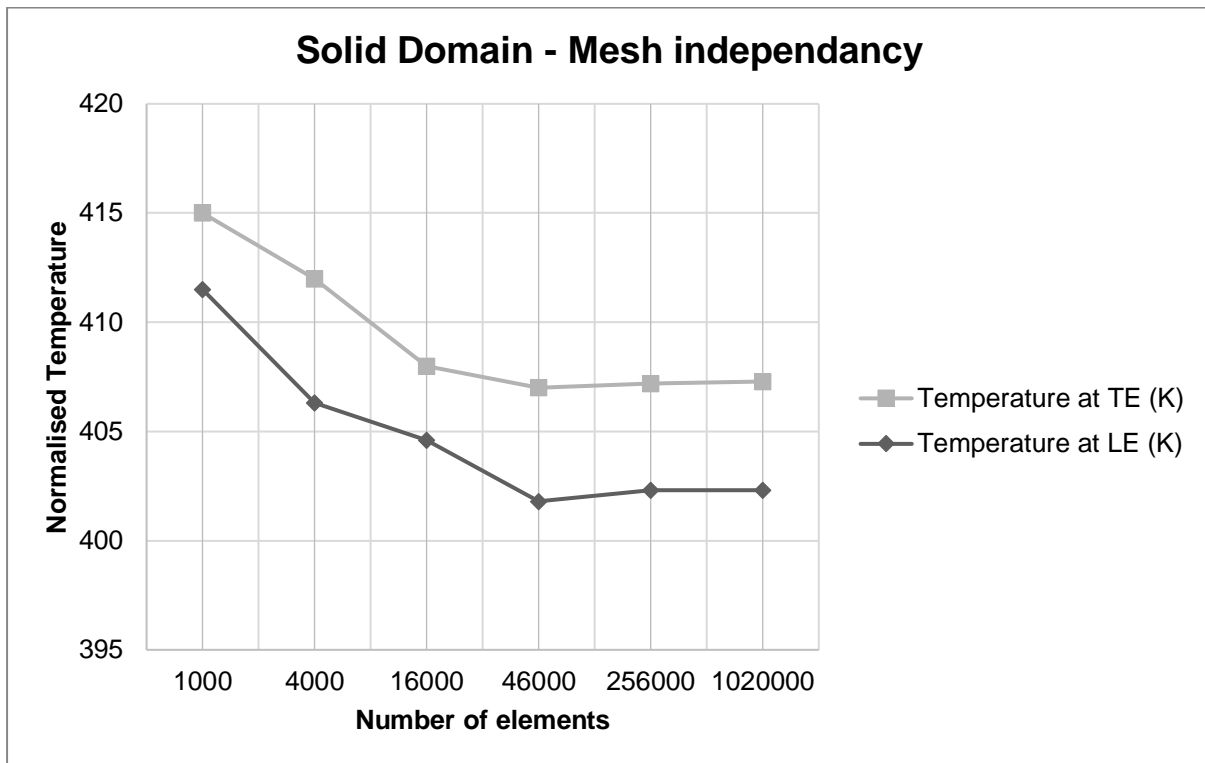


Figure 18: Lattice case solid domain mesh study

Whilst Figure 32 shows a varying temperature at the plate edges the maximum temperature is constant from 16000 elements. However, the large mesh sizing results in large gradients across the elements and so does not converge until 256000 elements.

Results

This section details the results of the lattice study in which the spacing and thickness of two parallel plates were varied across twenty CFD solutions. Table 16 below shows data taken from studies with a constant plate thickness of 9mm. The plate spacing however is varied from its nominal value of 168mm.

Table 13: Solution data for spacing variation with constant thickness

Parameters	Symbol	Units	Spacing									
			198	188	178	168	158	148	138	128	118	108
VARIABLES: Aerodynamic												
Total drag	F_{dT}	N	1222.6	1222.69	1222.7	1122.76	1077.89	1043.6	1079.5	1116.3	1150	1179
Upstream Mach Number	M_o	n/a	2.38	2.38	2.38	2.38	2.38	2.38	2.38	2.38	2.38	2.38
Downstream Mach Number	M_1	n/a	1.92	1.94	1.99	2.05	2.11	2.12	2.16	2.06	2.04	2.03
VARIABLES: Thermodynamic												
Maximum Plate Temperature	T_{\max}	K	410.6	410.6	410.5	410.7	410.7	410.7	410.8	411.3	411.7	412.2
Minimum Plate Temperature	T_{\min}	K	403.4	403.3	402.2	404.8	405.0	406.4	407.6	408.4	408.5	407.2

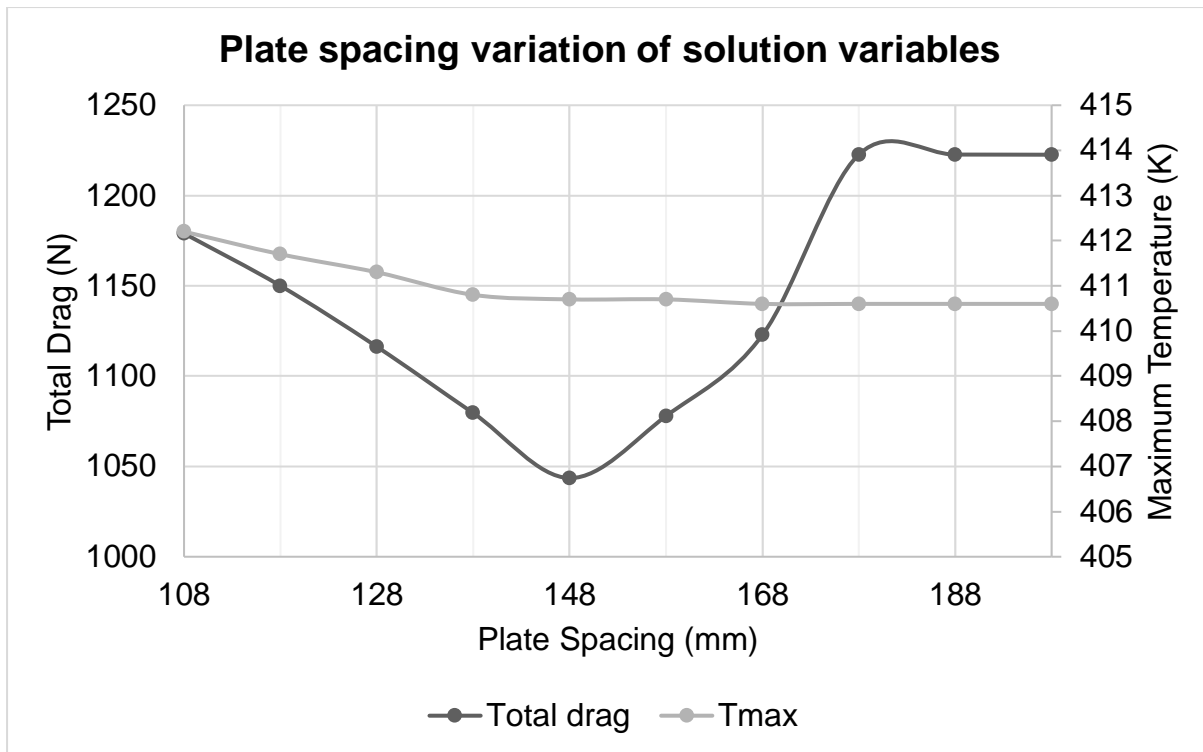


Figure 19: Solution variable variation with plate spacing

Table 17 and Figure 34 below feature results from studies with a constant plate spacing of 168mm, but thickness is varied from its nominal value of 9mm.

Table 14: Solution data for thickness variation with constant spacing

Parameters	Symbol	Units	Thickness (mm)									
			13	12	11	10	9	8	7	6	5	4
VARIABLES: Aerodynamic												
Total drag	F_{dT}	N	1480.6	1392.2	1304.9	1211.7	1125.0	1025	952.8	810.5	685.4	549.1
Upstream Mach Number	M_o	n/a	2.38	2.38	2.38	2.38	2.38	2.38	2.38	2.38	2.38	2.38
Downstream Mach Number	M_1	n/a	1.93	2.00	2.05	2.08	2.05	2.17	2.22	2.3	2.35	2.35
VARIABLES: Thermodynamic												
Maximum Plate Temperature	T_{\max}	K	411.6	411.5	411.3	411.3	410.7	410.9	410.7	410.2	410.1	409.5
Minimum Plate Temperature	T_{\min}	K	406.1	405.6	405.0	404.8	404.8	402.8	402.6	402.3	402.3	401.7

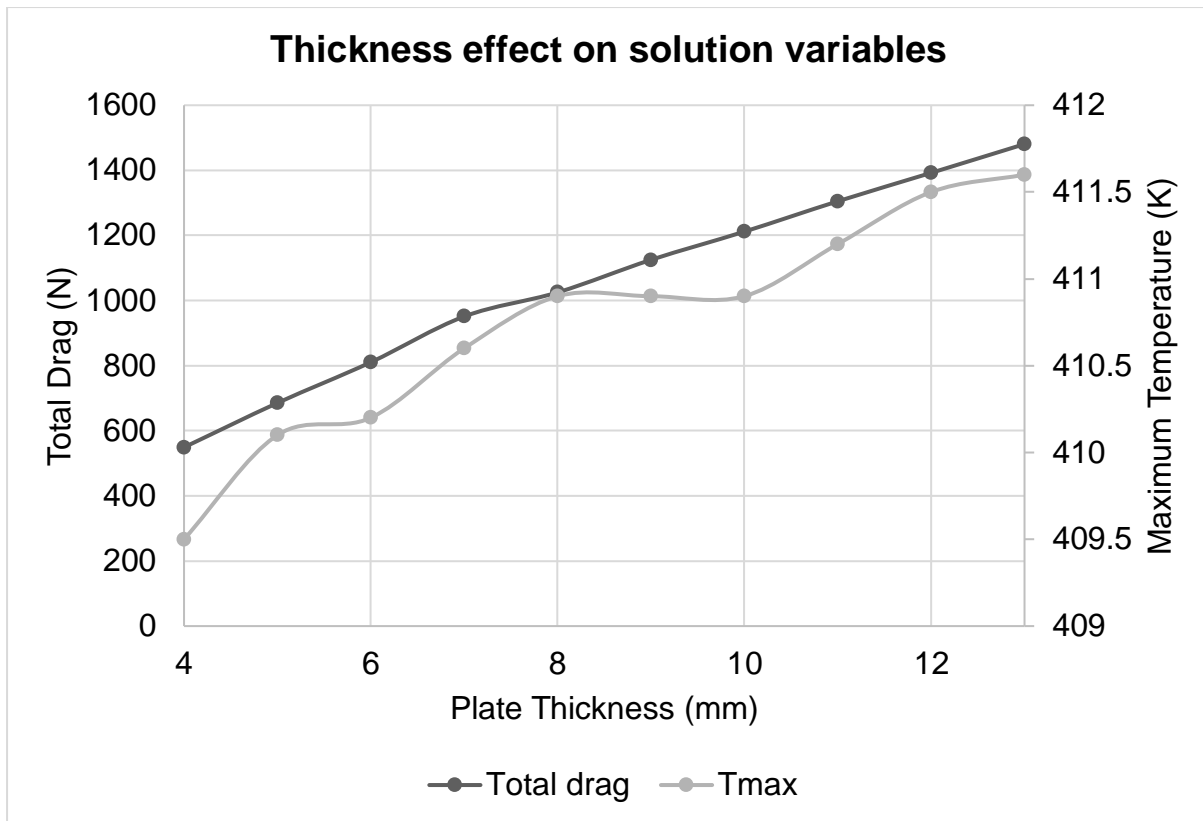


Figure 20: Solution variable variation with plate thickness

Discussion

The graphical representation (Fig. 33) of the spacing variation data suggests there is a “drag bucket” where downstream interference of the shock wave from the adjacent plate disturbs the flow at the TE and increases the local pressure. Figure 35, below, compares the pressure flow field at (a) 148mm plate spacing and (b) 178mm plate spacing.

The increase in pressure on the TE from the oncoming shock in Figure 35 (a) reduces the total drag by 180N, a 14.7% reduction from the drag at 178mm spacing. Therefore, to maximise pressure drag, efforts should be taken to design for minimum pressure at the TE. Accordingly, further reduction in plate spacing increases drag once more and results in a higher maximum temperature. Figure 36 (a) shows the pressure render (fluid domain) and the temperature renders (solid domain). Where the incident shock meets the plate a stagnation region is created (Fig. 35 (b)) causing large, localised conduction.

The drag begins to increase again in this case as the reflected shock no longer interferes with the TE pressure distribution. Thickness variation of the plate provides an unsurprising result: the thickness of the plate is proportional to the maximum plate temperature. This approximate linear relationship can be seen to be true for thicknesses of 4mm to 13mm (Fig. 34). Beyond this, however, a similar scenario occurs as shown in Figure 36.

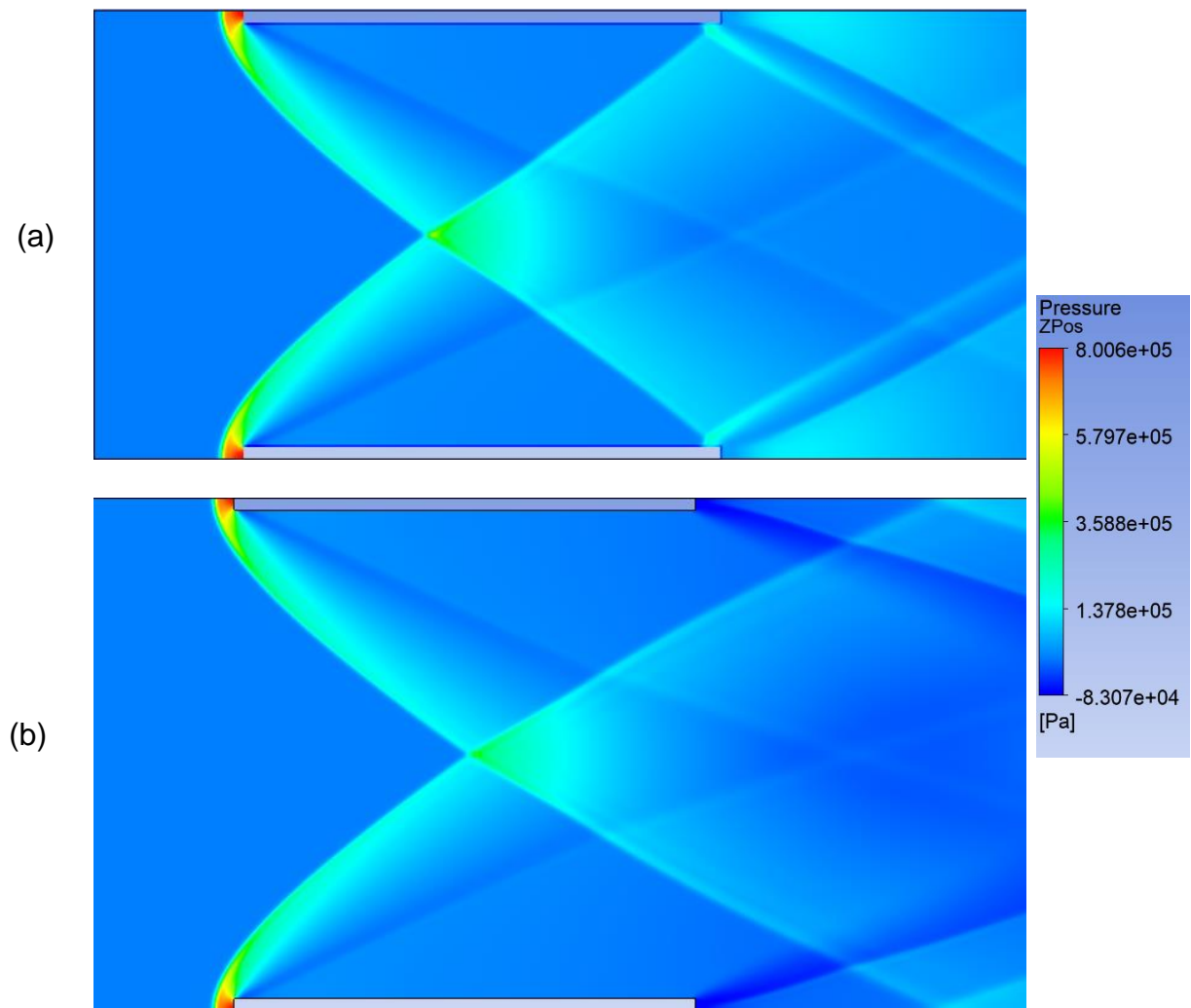


Figure 21: Pressure distribution across (a) 148mm plate spacing domain, (b) 178mm plate spacing domain

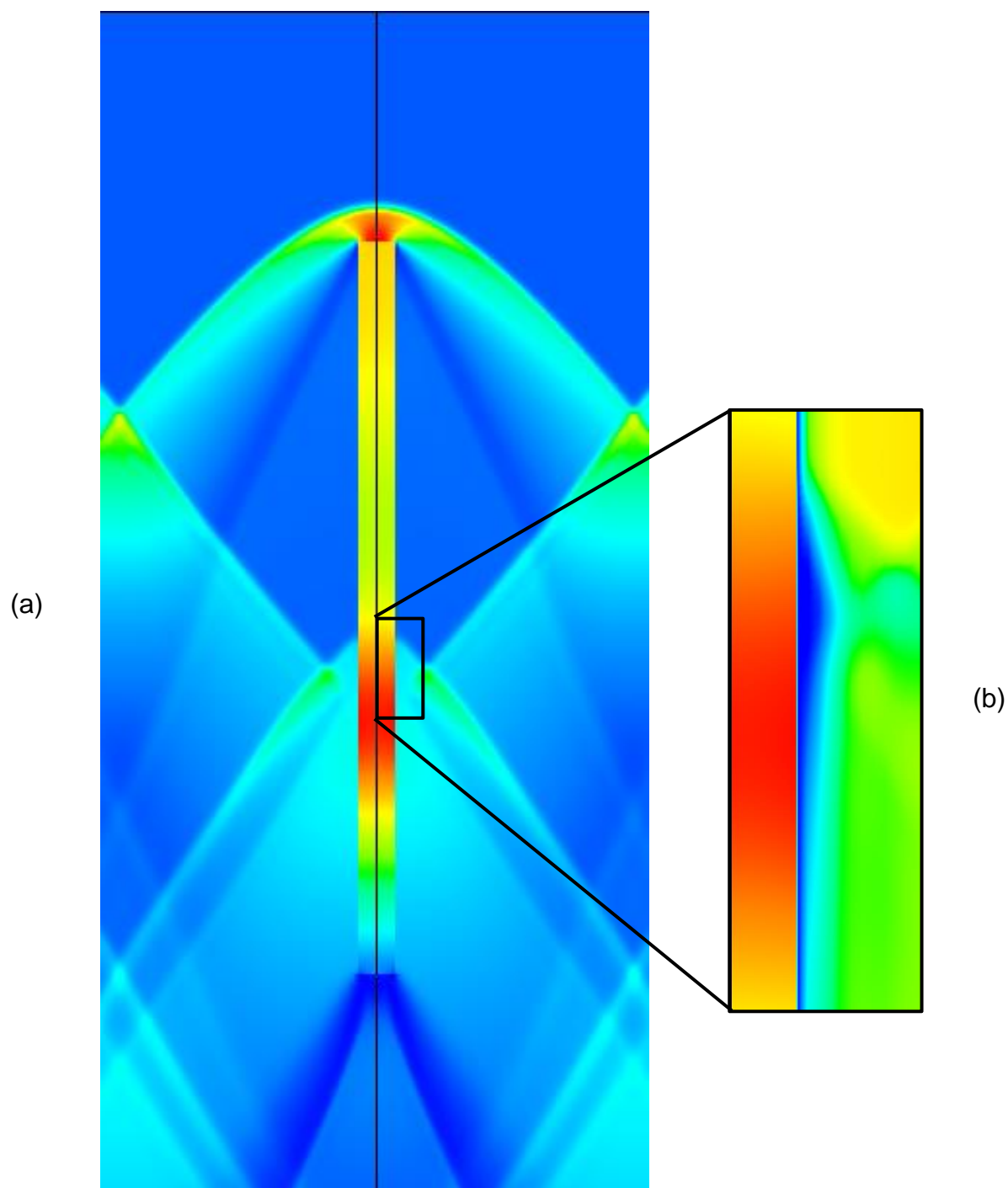


Figure 22: Shock wave interaction with adjacent plate: (a) Pressure contour of fluid and Temperature contour of solid, (b) Mach number contour at near wall region

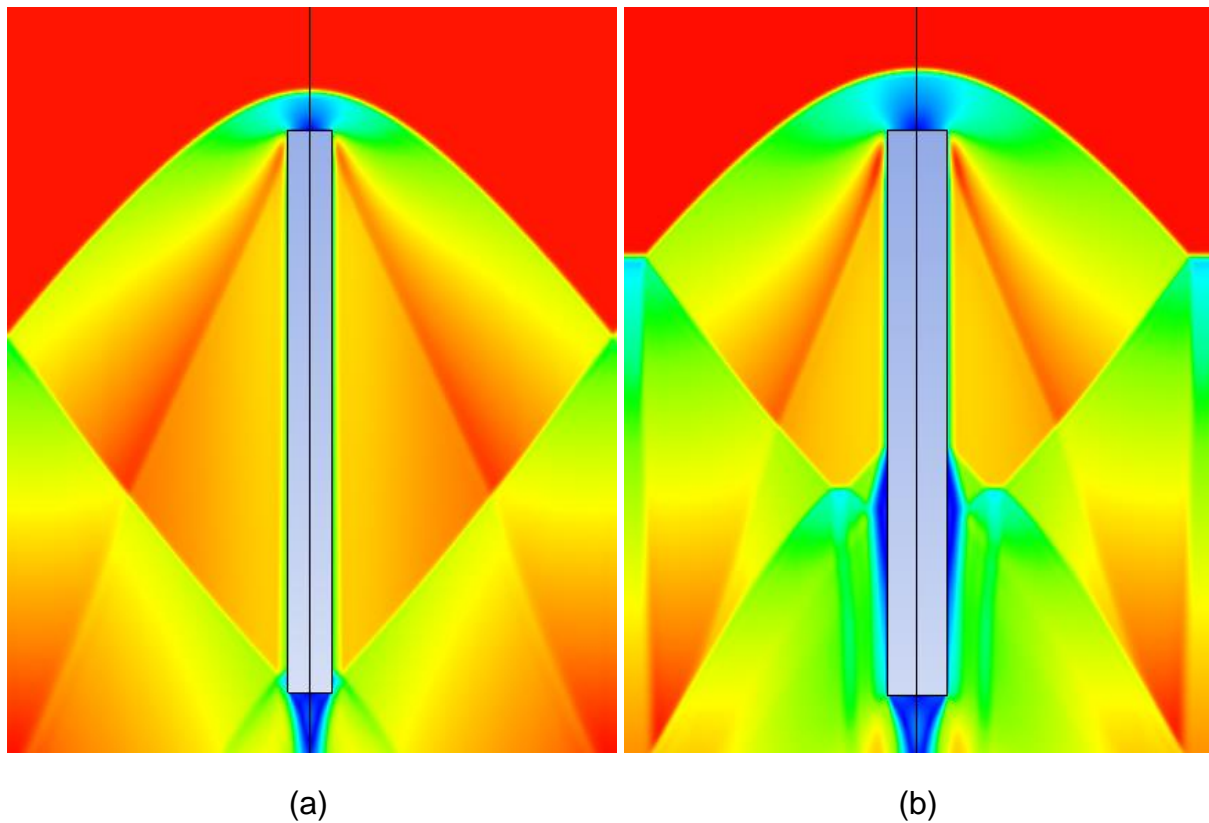


Figure 23: Rendering of Mach number for (a) 13mm thickness, (b) 20mm thickness

As the plate thickness increases the bow shock angle increases. Consequently, at 13mm plate thickness (a) the shocks become incident on the TE and at 20mm (b) it reflects off the plate causing localised heating.

Further to the maximum temperature, Figure 34 shows that plate thickness and drag have a linear relationship. Therefore, to maximise drag without causing localised heating at the TE, plate spacing should be increased whilst also increasing the plate thickness. A plate thickness of 10mm would be the optimal selection. Combining this selection with spacing thickness suggests 178mm would be a suitable separation.

Table 18 below, compares the drag and maximum temperature from solutions for the original grid fin dimensions and the suggested design improvements following the study. Noticeable increase in pressure drag – see TE of Figure 38 (a) and (b).

Table 15: Suggested design improvements to grid fin dimensions

Solution variable	Original design (9mm thick, 168mm spacing)	Suggested design (10mm thick, 188mm spacing)	Percentage increase
Total drag (N)	1125.0	1369.2	21.71%
Maximum temperature (K)	410.7	411.3	0.15%

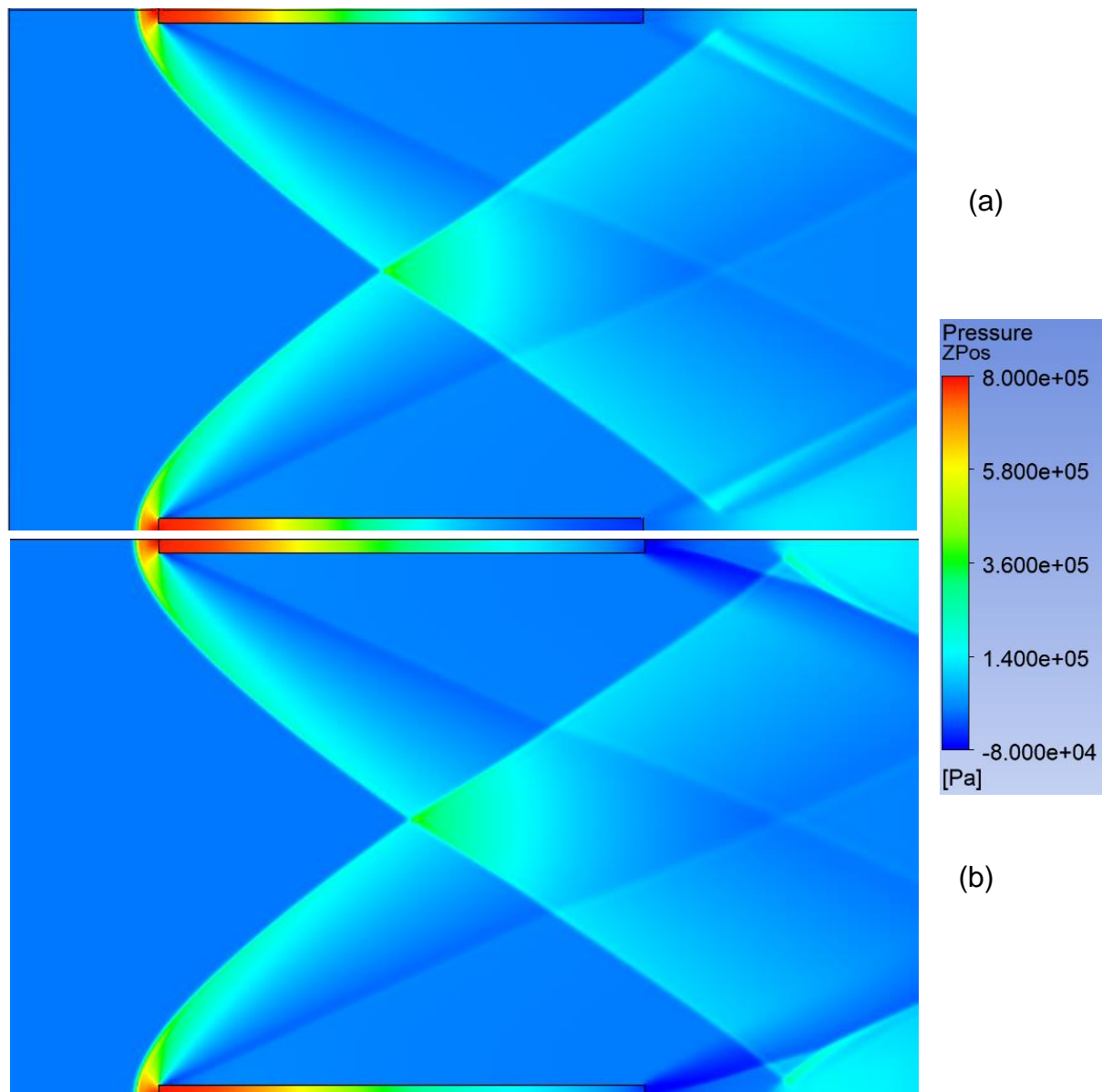


Figure 24: Pressure rendering of (a) Nominal design, (b) suggested design

Key Observations

The present 2D study would suggest that variation of sensitivity factors could increase grid fin drag with little to no consequence of maximum plate temperature. Further points of note:

1. Plate spacing has a complex relationship with max temperature and total drag. 148mm spacing is the critical value at which minimum drag is achieved, at 188mm spacing total drag and maximum temperature appear to reach a maximum and remain unchanged. However, decreasing the spacing from 148mm increases the maximum plate temperature.
2. Plate thickness has a linear relationship with total drag and maximum temperature.
3. Smaller thicknesses and larger spacing increase the total temperature range across the plate (Tab. 16 and 17).

4. The temperature range across all studies is very small, this suggests thermal conductivity and specific heat capacity of the solid domain are to be factored when considering composite integration.

3-dimensional cell study

The final study undertaken advances to 3-dimensions, now considering the spanwise flow over the grid fin. Aiming to investigate the shock interaction inside of a fin cell and compare the 3-dimensional differences and solution variables between the suggested design for 2 and 3D cases. Subsequently, the effect of thermal conductivity on the temperature distribution will be investigated by varying the constituent material of the solid domain using Aluminium 6061-T6, Titanium 6Al-4V and a polyamide CFRP (carbon-fibre reinforced plastic).

Method

Geometry and Meshing

The 3D model in this study is a simplification of the lattice structure of a grid fin (Fig. 39), one cell from its lattice is extracted and the flow through it is studied (Fig. 40). The computational domain as with the previous studies extends a $\frac{1}{4}$ a plate length upstream and 2.5 lengths downstream. The domain is discretised using the ANSYS-SpaceClaim Meshing tool into a tetrahedral dominant mesh with hexahedral elements in the near wall region.



Figure 25: Cell study geometry in the context of grid fin

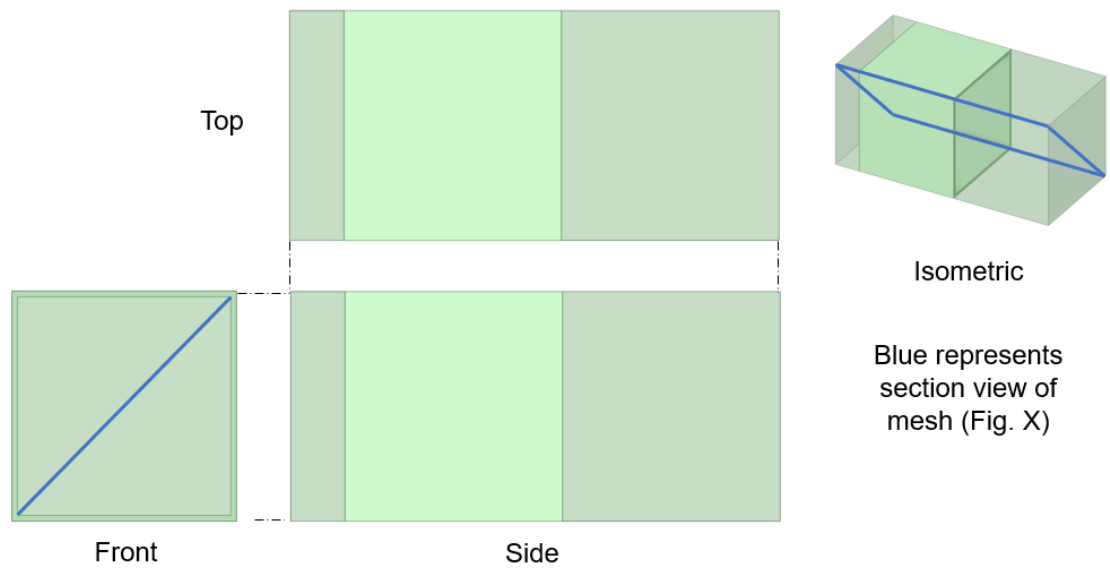


Figure 26: 3rd angle orthographic derived cell geometry in ANSYS-SpaceClaim

The red region highlighted in Figure 39 shows the derivation of geometry found in Figure 40. On which the blue lines represent the section view of the domain discretisation in Figure 41.

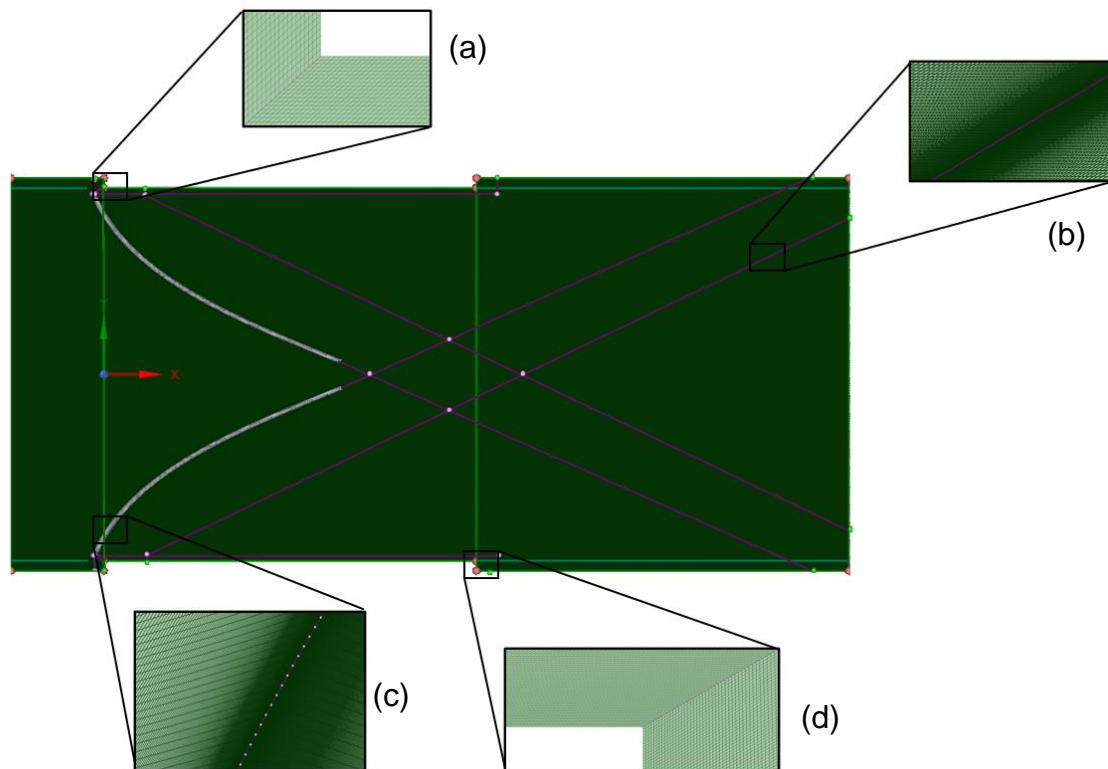


Figure 27: Hexahedral mesh in the domain with highlighted areas of interest: (a) Leading edge near-wall mesh, (b) Downstream oblique shock, (c) LE Bow shock, (d) TE near-wall mesh

- a) Mesh at LE, non-dimensional wall distance, $y^+ < 5.0$.
- b) Mesh at the downstream oblique shock, bias factor 10 away from the split line.
- c) Mesh at the bow shock, bias factor 10 away from the split line.
- d) Mesh at TE, non-dimensional wall distance, $y^+ < 15.0$.

Modelling Assumptions

No additional assumptions are made. Assumptions from previous studies still apply.

Setup

Solver settings are also identical to that of the 2D lattice study. Only amendments are to initialisation conditions to encourage convergence whilst considering variations in material properties (Tab. 19). Reliable solution is still assumed to be achieved at a residual of $1E-06$.

The material properties used for variation of the solid domain are shown below in Table 20.

Table 16: Cell study setup changes

Solid	Initialisation (t=0)	Option/Value	Units
Aluminium	Temperature	410	K
Titanium	Temperature	405	K
CFRP	Temperature	405	K

Table 17: Solid domain general and thermal properties

Property	Symbol	Unit	Titanium	Aluminium	CFRP
Molar Mass	M	kg/mol	47.87	26.98	13.07
Density	ρ	kg/m ³	4260	2730	1590
Specific Heat Capacity	c	J/kg K	520	1004	987
Thermal Conductivity	K	W/mK	17	169	1.2

Simulation Validity Study

As with previous studies, a full mesh sensitivity study was conducted; the domain is still assumed to be insensitive to sizing.

Table 18: Cell study fluid domain mesh study

Simulation no.	Total elements (million)	Elements at plate (million)	Total drag (N)	Maximum Plate Temperature (K)
1	3.0	0.466	1781	403.8
2	12.1	1.32	2122	406.2
3	28.7	1.98	2130	407.3
4	36.4	2.37	2122	407.2
5	49.0	3.24	2116	407.2

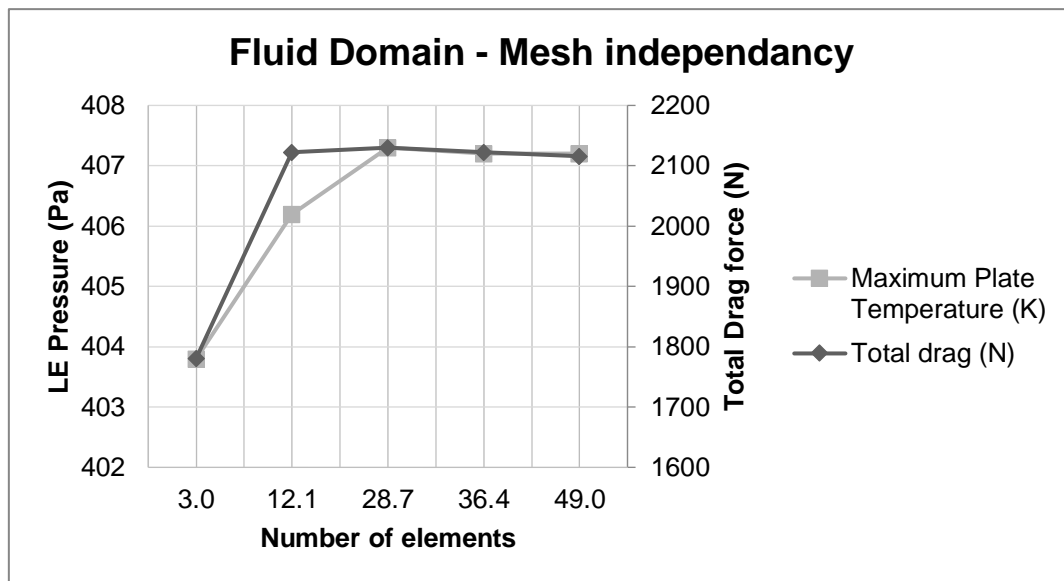


Figure 28: Cell study fluid domain mesh study

Table 19: Cell study solid domain mesh study

Simulation no.	Total elements (million)	Temperature at LE (K)	Temperature at TE (K)
6	0.3	411.5	415
7	0.6	406.3	412
8	1.2	402.4	408.5
9	1.8	402.3	407
10	2.0	402.3	407.2
11	2.4	402.3	407.3

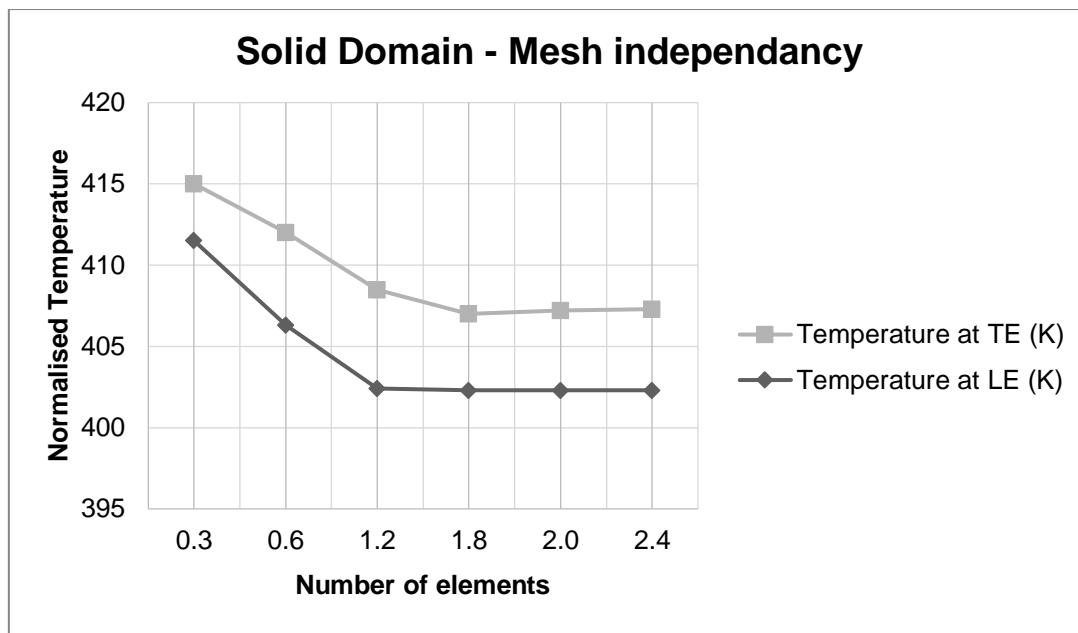


Figure 29: Cell study fluid domain mesh study

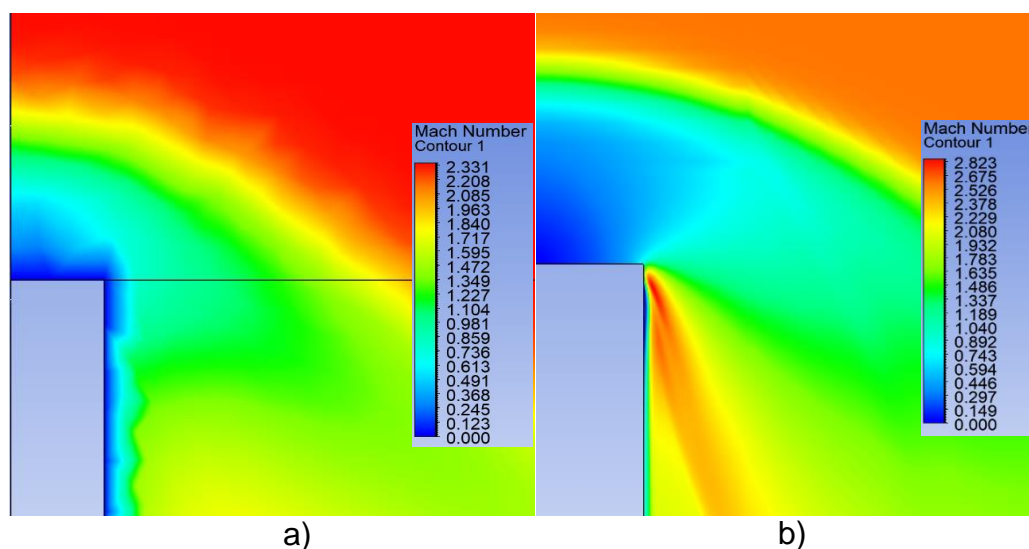


Figure 30: Comparison of variable resolution for: (a) 3 million elements, (b) 28.7 million elements

Figure 44 shows the importance of mesh independency studies, assuming mesh has no impact on the solution would have resulted in poor resolution of the boundary layer and no evolution of the oblique shock seen in Figure 44 (b).

Results

Figure 45 below presents the difference seen in the flow field as the study of 178mm spacing with 10mm thickness progresses from (a) 2D to, (b) 3D. Table 23 gives the solution variables.

Table 20: Solution variable differences in 2D and 3D

Study	Drag (N)	Percentage change	Maximum Temperature (K)	Percentage change
2D	1369.2	85.77%	411.3	-0.66%
3D	2543.6		408.6	

Figures 46 and 47 below show that there is no discernible difference in temperature distribution between the CFRP and titanium plates. Whereas aluminium has a higher and more constant temperature profile.

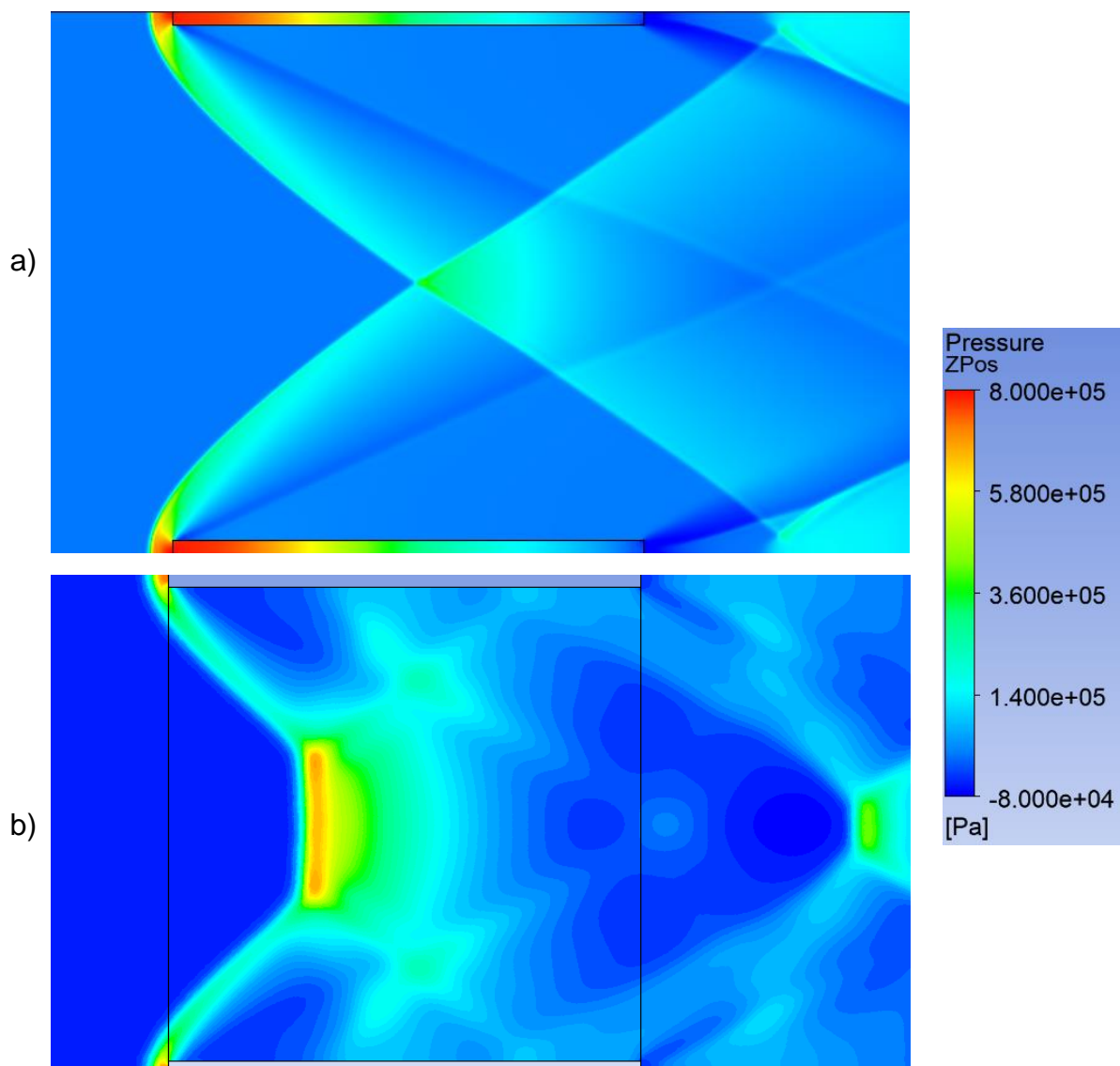


Figure 31: Equivalent pressure render of 178mm/10mm in: (a) 2D, (b) 3D

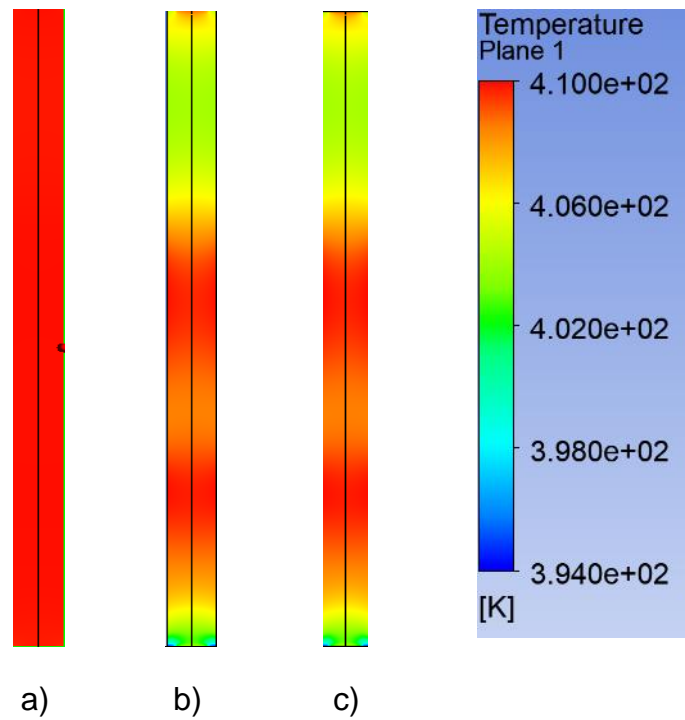


Figure 32: Temperature distribution along XZ plane in plates: (a) Aluminium 6061-T6, (b) Titanium 6Al-4V and (c) polyamide CFRP

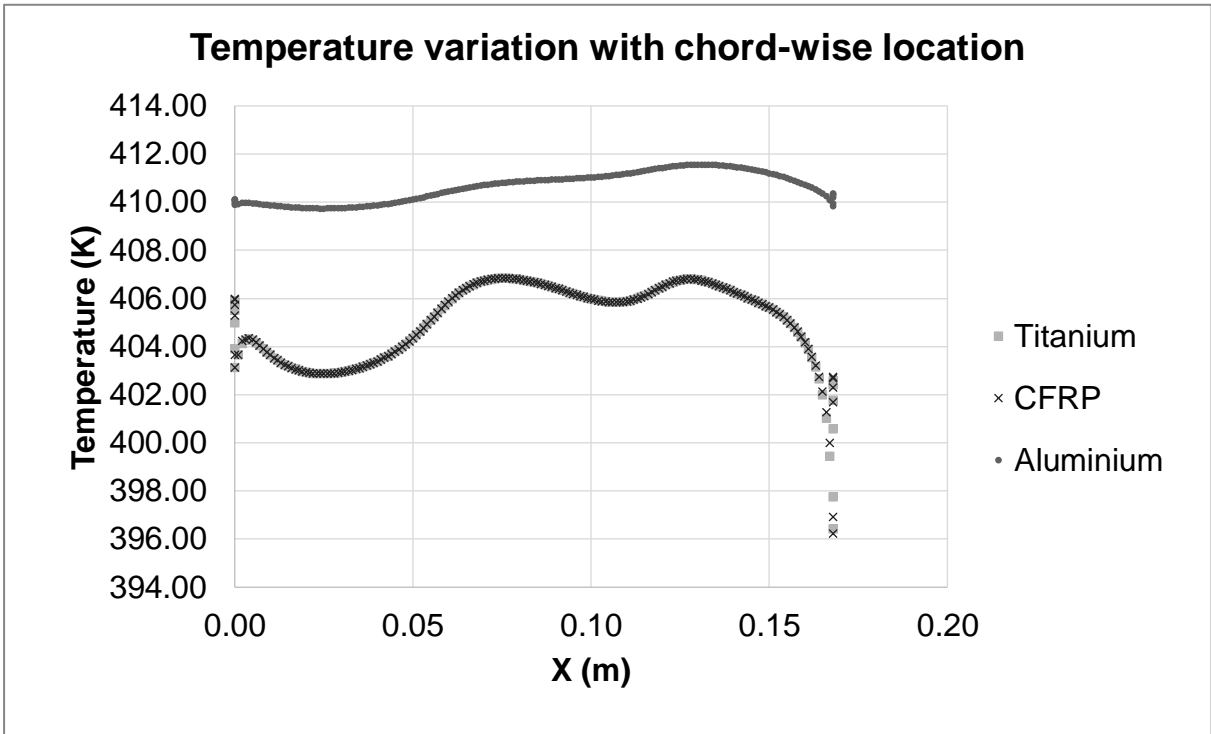


Figure 33: Temperature variation in different plate materials

Discussion

As expected, progressing to 3-dimensions has vastly increased the total drag whilst the maximum temperature has been mostly maintained. Interface temperature has remained unchanged as the air temperature cannot exceed 417K without changing the fundamental system; since the scenario we are considering is a steady-state (time-independent) solution and therefore the essential inlet condition doesn't change; the maximum achievable temperature within the fluid domain is simply a component of its pressure and general properties (density and specific heat) in any given finite volume. Beyond this one main difference occurs, a normal shock develops (Fig. 45 (b)). The presence of this normal shock disturbs the downstream flow pattern that the suggested design (Fig. 45 (a)) intended to invoke. As a result of the downstream disturbance, localised heating as seen in Section 5.3 Figure 36 occurs. To avoid such heating, the plate spacing should be increased further. The variation in plate conductivity plays a vital role in the interface temperature. Figure 47 shows the chord-wise distribution of temperature for the three cells of different materials. There is little-to-no variation in the titanium and CFRP plates, considering their similar thermal conductivities this is expected. Unlike aluminium which is heated closer to the maximum fluid temperature. Whilst the temperature distribution of the plates can be accurately estimated from 2-dimensional solutions, the solution fails to provide reliable insight into the flow field that pertains to the 3D case. This stems from the variation in shock interaction and the choking of flow in the 3D case causing the normal shock development.

Key Observations

1. Higher thermal conductivity, as in aluminium, results in a smaller temperature range and an increased maximum temperature.
2. Maximum plate temperature is limited by the max fluid temperature.
3. Large percentage difference in total drag between 2D and 3D, pertaining to the normal shock development in 3D cases and increased frontal area.
4. There is a negligible difference between the temperature profile of titanium and CFRP cells.
5. 2D cases fail to give accurate insight into the solution of 3D geometry in the same flow.

Material Selection

Following the comparison of the suggested geometry in 3 dimensions and the material variation of the solid domain the structural feasibility of the materials can be investigated. This will be done using simplified geometry for cantilever bending equations to assess whether the bending stress exceeds the von Mises theory for maximum bending stress. This will follow the fundamental background knowledge essential to understanding the physics and material science of the present section.

Background Information

Composite Theory

Composite materials consist of two or more different materials, comprised of two distinct 'phases': a reinforcement, and a matrix (Fig. 48). Composites are commonly categorised by their matrix phase into, fibre-reinforced polymers (FRP), metal matrix composites (MMC), and ceramic matrix composites (CMC). A CFRP is a subsection of FRPs with a polymer matrix and carbon reinforcement phase. Due to carbon fibres

being so light their specific strength (strength per unit mass) is superior to traditional materials. This, along with their high stiffness, results in them being the fibre of choice for composites in high-stress applications (Shrivastava, 2018).

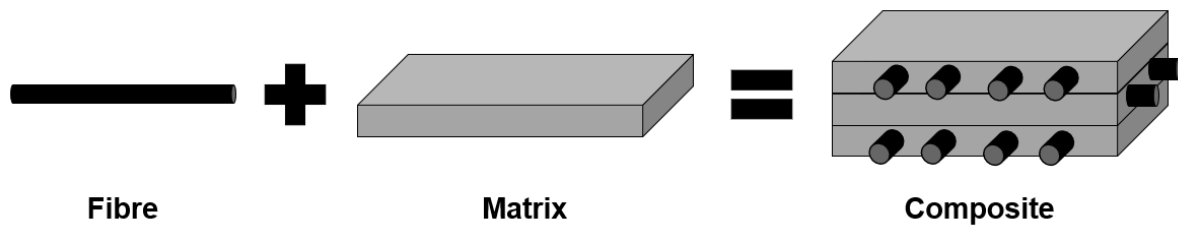


Figure 34: Composite schematic

The polymer matrix of an FRP may also be varied: epoxy, phenols and amides are common examples. The selection of matrix and fibre results in hundreds of combinations, each with different mechanical and thermal properties. Figure 49 shows the variation of maximum service temperature with thermal conductivity for different matrix, reinforcement combinations.

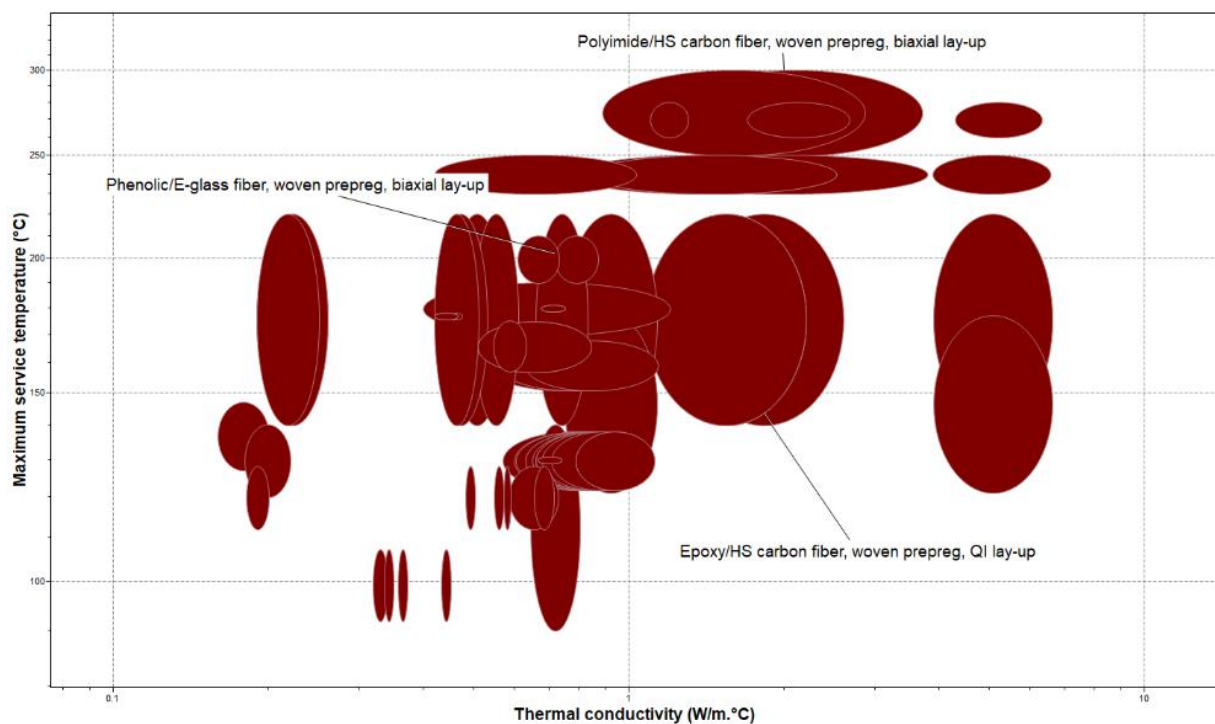


Figure 35: Thermal conductivity against Maximum service temperature created using Ansys Granta (2022)

Bending Theory

Bending or, flexure is a mechanics problem where a structural element is subject to a force perpendicular to its axis. A cantilever is a structural element that is fixed at one end and unsupported at the other. Consequently, when loaded the cantilever carries the load to the supported end applying a bending moment and shear stress.



Figure 36: Cantilever beam schematic, point load

In the simplest case (Fig. 50), the bending moment and maximum stress can be expressed as:

$$\text{Maximum Bending Moment, } B_{max} = B_A = -FL \quad (8)$$

$$B_A = \text{maximum moment in A (Nm)}$$

$$L = \text{length of beam (m)}$$

$$\text{Maximum Bending Stress, } \sigma_{max} = \frac{By}{I} \quad (9)$$

$$\sigma = \text{stress (Pa (N/m}^2\text{))}$$

$$y = \text{distance to surface from neutral axis (m)}$$

$$M = \text{bending moment (Nm)}$$

$$I = \text{second moment of area (m}^4\text{)}$$

In the context of this work, a uniformly distributed load will be applied to the cantilever (Fig. 51).

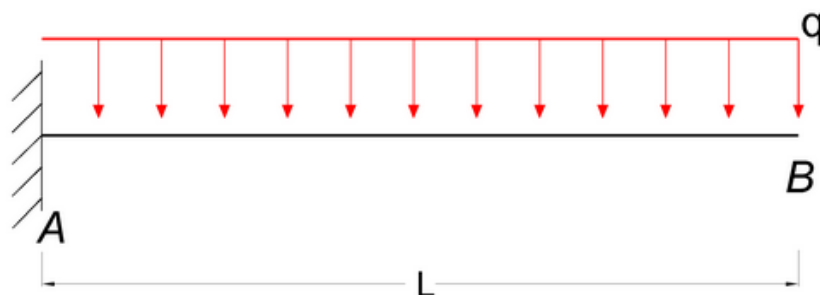


Figure 37: Cantilever beam schematic, distributed load

A cantilever experiences its maximum bending moment at the wall fixture, which is expressed by B_A , (Eq. 10).

$$B_A = -\frac{qL^2}{2} \quad (10)$$

$q = \text{distributed load (N/m)}$

The maximum moment in a cantilever beam is at the fixed point and the maximum stress can be calculated by combining *Equations (9) and (10)*:

$$\sigma_{\max} = \frac{y(-\frac{qL^2}{2})}{I} \quad (11)$$

These equations can be used in conjunction with the yield strength of the materials to calculate a factor of safety (FoS).

Method

Setup

Bending moments and stresses are independent of material properties, depending only on the beam geometry. Thus, the 3 cases are modelled as in Figure 52 (a) below.

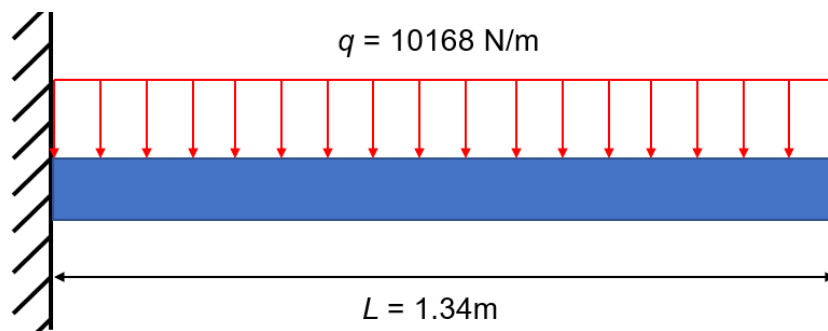
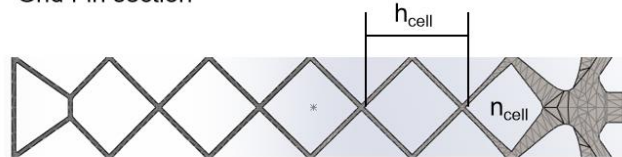


Figure 52: (a) Cantilever beam setup

To arrive at this simplification though a number of assumptions are to be made:

1. The beam is a volume weighted average of the cells along the centreline
2. The total drag from 3-dimensional cell study is then applied along the equivalent cell height in the simplification

Grid Fin section



Bar simplification

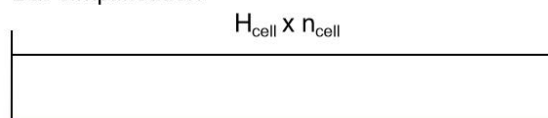


Figure 52: (b) Grid fin to bar simplification

Essentially each cell and its drag has been transformed into a single bar representative of its height.

Beam dimensions:

$$L = 0.168\text{m}$$

$$h = 0.168\text{m}$$

$$t = 0.01\text{m}$$

$$\text{Second moment of area, } I_{xx} = \frac{th^3}{12} \quad (12)$$

$$\text{Second moment of area, } I_{yy} = \frac{ht^3}{12} \quad (13)$$

$$I_{xx} = 3.95\text{e-}6 \text{ m}^4$$

$$I_{yy} = 1.4\text{e-}8 \text{ m}^4$$

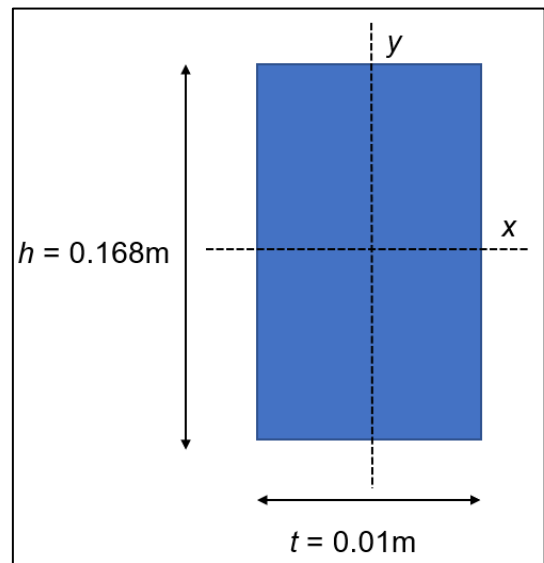


Figure 53: Second moment of area from bar cross-section

Modelling Assumptions

1. Cantilever model would assume the grid fin is joined perfectly to Falcon 9's body and thus the bending moment occurs at the wall (rocket body).
2. The beam is assumed to be straight and of constant cross-section.
3. The beam assumes that no other cell from the grid fin lattice increases its resistance to deformation (bending).
4. The elastic limit E (Young's Modulus) is assumed to be equal in both tension and compression (NOTE: It is known that this is not true for CFRP as it is not a homogenous material).
5. The geometry used assumes that the structural element fails in bending and not buckling.
6. All materials are without additives or coatings, this will affect the results of aluminium as in spaceflight operations as standard, uses an anodic oxide coating that has specific thermal properties.
7. Composite materials are assumed to have perfect fibre volume fraction (no voids) and all fibres are aligned with their axis perfectly.

Results

To calculate the FoS, the bending moment and shear forces must be converted to principal stresses (Tab. 24).

Table 21: Calculations of 2D principal stresses

Property	Symbol	Value	Units	Formula
Bending Stress	σ_y	153498187.3	Pa	Equation 11
Direct Stress	σ_x	0	Pa	n/a
Shear Stress	τ_{xy}	72440000	Pa	$\tau_{xy} = \frac{VQ}{Ib}$ (14)
Principle Stress 1	σ_1	1.49E+08	Pa	$\sigma_1 = \left(\frac{\sigma_x + \sigma_y}{2}\right) + \sqrt{\left(\frac{\sigma_x - \sigma_y}{2}\right)^2 + \tau_{xy}^2}$ (15)
Principle Stress 2	σ_2	4.31E+06	Pa	$\sigma_2 = \left(\frac{\sigma_x + \sigma_y}{2}\right) - \sqrt{\left(\frac{\sigma_x - \sigma_y}{2}\right)^2 + \tau_{xy}^2}$ (16)
Bending Stress	σ_{y_MPa}	153.4981873	MPa	$\frac{\sigma_y}{10^6}$
Direct Stress	σ_{x_MPa}	0	MPa	$\frac{\sigma_x}{10^6}$
Shear Stress	τ_{xy_MPa}	72.44	MPa	$\frac{\tau_{xy}}{10^6}$
Principle Stress 1	σ_{1_MPa}	149.1890931	MPa	$\frac{\sigma_1}{10^6}$
Principle Stress 2	σ_{2_MPa}	4.30909418	MPa	$\frac{\sigma_2}{10^6}$

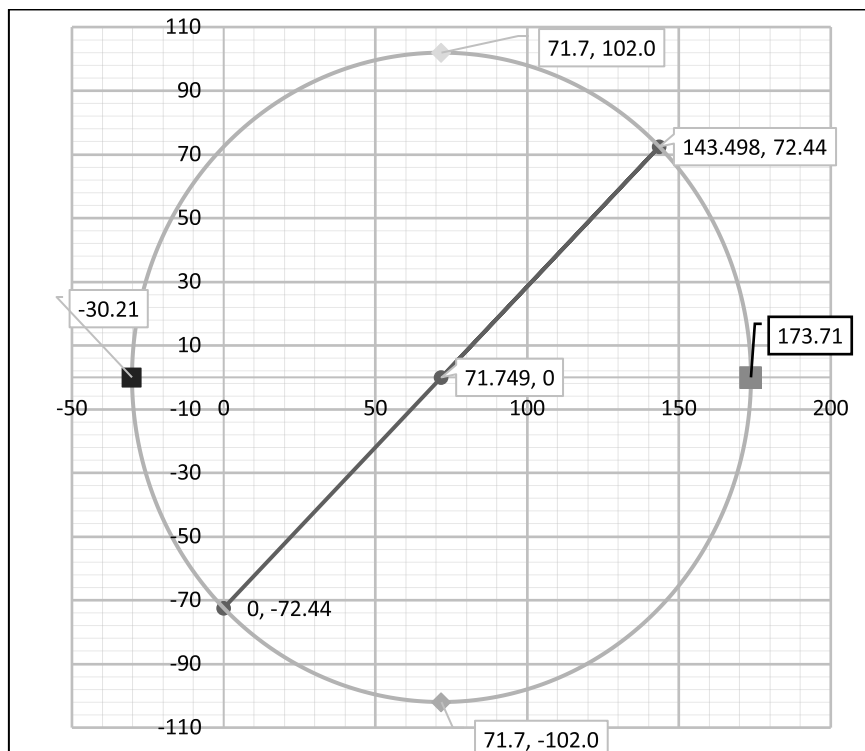


Figure 38: Mohr's circle for 2D principal stresses on the cantilever beam

Considering the combined stresses in 3 dimensions:

Table 22: Calculations of von Mises stress

Property	Symbol	Value	Units	Formula
Principle Stress 1	σ_1	1.49E+08	Pa	Eq. (15)
Principle Stress 2	σ_2	0	Pa	n/a
Principle Stress 3	σ_3	4.31E+06	Pa	Eq. (16)
Von Mises Stress	σ_{vM}	1.47E+08	Pa	$\sqrt{\left(\frac{(\sigma_1-\sigma_2)^2+(\sigma_2-\sigma_3)^2+(\sigma_3-\sigma_1)^2}{2}\right)}$ (17)
Principle Stress 1	σ_{1_MPa}	149.2	MPa	$\frac{\sigma_1}{10^6}$
Principle Stress 2	σ_{2_MPa}	0	MPa	$\frac{\sigma_2}{10^6}$
Principle Stress 3	σ_{3_MPa}	4.31	MPa	$\frac{\sigma_3}{10^6}$
Von Mises Stress	σ_{vM_MPa}	147.1	MPa	$\frac{\sigma_{vm}}{10^6}$

The von Mises yield criterion calculated above (Tab. 25) is employed to calculate the yielding of materials under complex loading. It is only applicable to ductile materials, aluminium. Brittle materials such as CFRP and titanium have their yield strengths compared to the principal stresses.

The final consideration for this method is the variable yielding of materials with temperature. For all but a small few, materials yield strength decreases as temperature increases (Fig. 55).

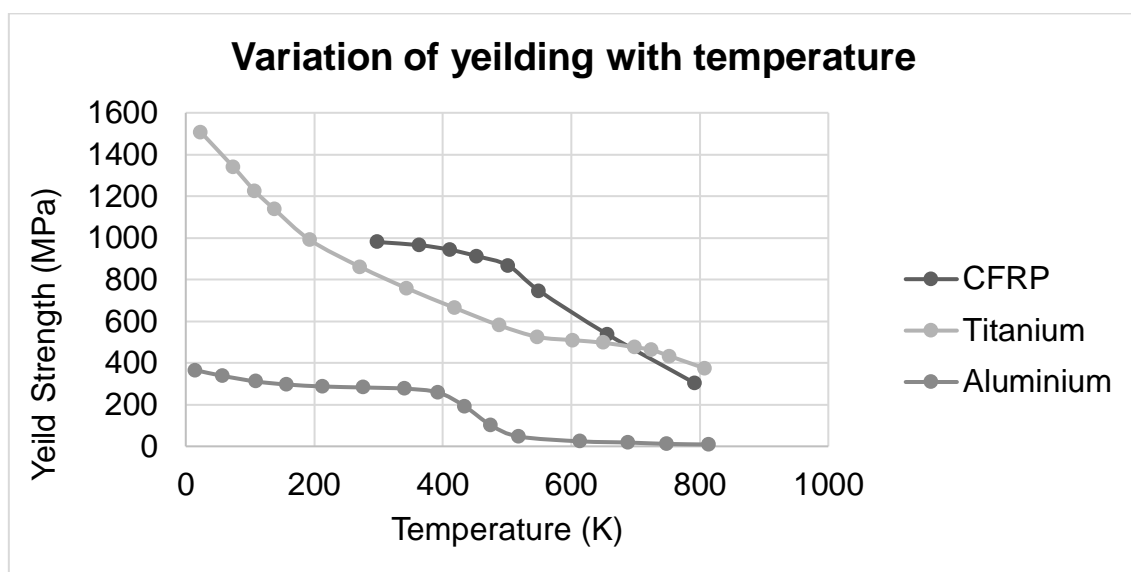


Figure 39: Variation of yield stress with temperature (ANSYS-GRANTA, 2021)

Therefore, by considering the variation of yielding there is expected to be a vast impact on the FoS calculations. Table 26 shows the yielding at ambient conditions and under thermal loading in the previous studies.

Table 23: Comparison of yield strength at ambient and study conditions

Material	Yield at 298K (ambient)	Yield at 410K (study)	% Difference
Aluminium (Al)	280.4	212.3	27.6
Titanium (Ti)	860.6	663.1	25.9
CFRP	980	917	6.64

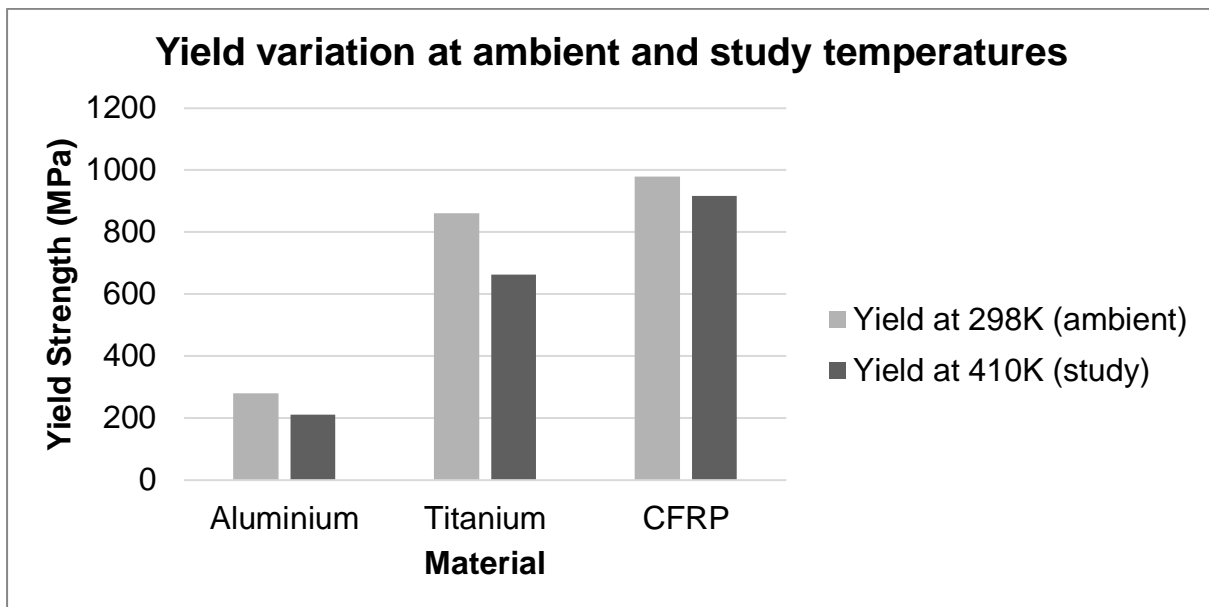


Figure 40: Comparison of yield strength at ambient and study conditions

Considering these effects on the yield strength, the FoS for the different conditions can be calculated:

Table 24: Calculation of FoS at different temperatures

Temperature (K)	Material	Theoretical yielding (MPa) [Tab. 25]	Yield strength (MPa)	FoS
298.15 (Ambient)	Al	147.1	280.4	1.91
	Ti	149.2	860.6	5.77
	CFRP	149.2	980	6.57
410 (Study)	Al	147.1	212.3	1.44
	Ti	149.2	663.1	4.44
	CFRP	149.2	917	6.14

Discussion

Space X, under the guidance of the Federal Aviation Authority (FAA), follows a minimum FoS for all spaceflight operations of 3.00. Under the assumptions of this study therefore, and the loading conditions obtained from the spacing/thickness variation study, Aluminium 6061-T6 is not a viable option for optimisation of the grid fins (Tab. 27). Titanium and CFRP, however, offer superior yield strength under the thermal and static loading conditions allowing for further optimisation of the design. Parametric goal-seek calculations of the principal stress σ_1 , suggest drag could be increased across the assumed grid fin span (Fig. 52 (b)), or across each cell whilst maintaining a FoS of 3.00.

Table 25: Total drag from a beam of cells

Material	Total Drag from beam span	Drag per cell
Titanium	19685N	2812N
CFRP	30894N	4413N

Whilst the polyamide CFRP looks to give superior FoS to titanium, its orthotropic nature should be considered. Depending on the direction load is applied, the CFRP will react differently. This is also dependent on the fibre orientation, the CFRP in question here has a biaxial layup and would exert the following properties (Tab. 29):

Table 26: Comparison of strength of CFRP under different loading conditions

	Tensile	Compressive	Flexural
Strength (MPa)	910	685	910

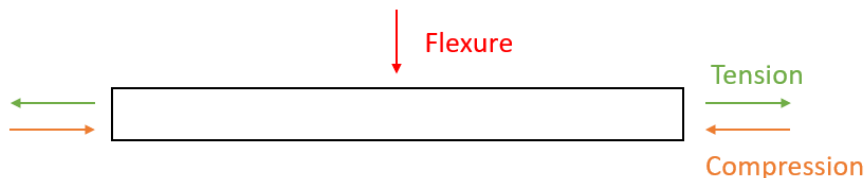


Figure 41: Different loading conditions on a composite beam

Resultingly, the layup of each laminate ply and its fibre orientation will greatly impact the FoS and should be further investigated but does initially suggest superior feasibility to titanium. Secondly, under the study conditions (410K) carbon fibres yield is higher than titanium's, however, its gradient of variation is steeper and by 700K titanium offers superior yield strength – this is not a temperature outside the realm of possibility for a grid fin in all operating conditions.

Furthermore, assumptions such as no void volume in the composite in a practical sense are unachievable. Affecting both the FoS calculations and potentially having far-reaching practical implications when considering the environmental cyclical loading of the grid fin – ambient temperature and pressure to re-entry and vacuum conditions.

Overall Performance

The solutions to the cell, *2-dimensional lattice study – Results*, predicted a 464N increase in total drag when the spacing and thickness were adapted to 178mm and 10mm respectively. For a grid fin consisting of 50 grid cells, a total drag of 12715N would be produced (an increase of 21% from the original design). This increase in drag would aid in slowing descent but in comparison to the engines and the Falcon 9 body produce little drag force, potentially saving 0.1-0.5% of the fuel used in re-entry. Even this small fraction amounts to 572kg minimum saved in kerosene and liquid oxygen, equating to approximately £60,000 in savings by mass (£120/kg (SpaceX, 2022) and additional savings for fuel costs.

However, the potential for the greatest cost savings stems from mass reduction at lift-off (Tab. 30).

Table 27: Calculations of material cost and mass

Property	Symbol	Current design (168mm/9mm)	Suggested design (178mm/10mm)	Units	Formula
Cell volume	V_{c_mm}	1.01E+06	1.26E+06	mm ³	$(S^2 + 2t) - S^2$
Cell volume	V_c	1.01E-03	1.E-03	m ³	$\frac{V_{c_mm}}{10^9}$
Grid volume	V_G	0.054	0.063	m ³	$50(V_c)$
CFRP cost		10800	12600	£	$V_c \left(\frac{£}{m^3} \right)$
Titanium cost		4816.80	5619.60	£	$V_c \left(\frac{£}{m^3} \right)$
CFRP mass	m_{CFRP}	88.02	102.69	Kg	$V_c \rho_{CFRP}$
Titanium mass	m_{Ti}	239.22	279.09	Kg	$V_c \rho_{Ti}$

Currently, Falcon 9 costs £120 per kilogram to be inserted into a low earth orbit. Reducing the grid fin mass to 88.02kg for the original design would save £62000 per flight, Realistically, it would generate even more revenue as the weight saved can be designated to extra payload which costs (SpaceX, 2022) £5500/kg compared to the true reduction of £120/kg.

Conclusions

Aiming to increase the cost-effectiveness of reusable launch vehicles this paper investigated the effects of design factors on grid fin performance in 2 and 3 dimensions. Progressing from validation of previous literature to application of 3-dimensional computational results to structural mechanics of materials.

The validation against Tekure's literature and White's oblique shock model proved essential in ensuring correct physics and solver were selected before progressing onto complex geometry. The baseline study demonstrated that whilst the temperature distribution through the plate, using the suggested conjugate solver for thermal energy were within a 5% error margin, the location of peak temperatures could vary through shock development and could lead to localised conduction.

After validation, geometric sensitivity factors to drag and maximum temperature were investigated in 2 dimensions. It was discovered that a critical value for plate spacing

exists where interference of the bow shock from the adjacent plate constructively interferes with the trailing edge decreasing the pressure drag. The study also showed evidence of a linear relationship between plate thickness and drag/temperature. From this a suggested design of 178mm spacing, 10mm thickness was derived producing 21.7% more drag than the original geometry with a 1 Kelvin temperature increase.

The final study used this derived geometry to identify the maximum temperature and total drag in 3 dimensions. The 3D study proved to vary greatly from its 2D simplification due to the development of a normal shock within the cell. These results were then applied to beam bending theory, utilising the assumption of a wall-supported cantilever with a uniformly distributed load to calculate a FoS for Aluminium, CFRP and Titanium at ambient and elevated temperatures. Whilst proving that a polyamide CFRP would provide a FoS of 6.14 it would require huge research and development costs but is an exceptional long-term investment, saving £62,000 per flight. The suggested geometry with titanium or CFRP would save £40,000 per flight due to the increased mass of each fin from the increased plate thickness.

Despite all this, the steady-state nature of this investigation is a far-reaching limiting factor on the impact of the solution data obtained. The effects of the design factors investigated were ultimately only tested for an instantaneous moment of Falcon 9's flight. This poses the question of whether a transient solver with variable inlet conditions could better predict the impact of the sensitivity factors over a larger portion of flight. Alternatively, using the suggested improvements to the geometry, steady-state computations could be carried out at different Mach numbers.

Furthermore, composite materials are a vastly complex yet still developing field of material science. This project suffers from a lack of depth in their feasibility as a replacement for traditional materials. Without an in-depth insight into the manufacture and lifetime of a composite fin as well as their true mechanical properties (no assumptions), there is a limit to how justifiable the development and subsequent maintenance costs are but could prove an interesting additional study.

Further considerations

It is becoming more and more important to consider the environmental impact of everything we do and suggest improvements for future studies. Furthermore, in a time of crisis regarding the energy sector, power consumption and usage times are especially relevant to big CFD studies. Table 31 and 32 below, highlights the impact of this research alone.

Table 28: Total simulation time per method

Study	Number of runs	Total iterations	Accumulated time
Validation	32	27423	323 hrs
Lattice	15	11071	212 hrs
Cell	12	3781	389 hrs
Total	59	42275	924 hrs

The University of Plymouth computer hardware uses Intel(R) Core (TM) i5-7500T CPU @ 2.70GHz processors which when utilised for CFD studies using 4 cores consumes 111W under full load.

Table 29: Economic and environmental impact of study

Parameter	Value	Units
Power consumption	111	W
Energy price	0.29	£ / kWh
Usage time	924	Hrs
Power consumed	111.804	kWh
Cost	32.42	£
CO2 produced	43.01	Kg

Whilst this doesn't consider the time spent in other software or time spent discretizing and setting up the CFD studies the total CO2 produced is equal to that of driving a car for 210 miles.

References

- Akansu, Y., Sarioglu, M., Kuvvet, K. and Yavuz, T., (2008). Flow field and heat transfer characteristics in an oblique slot jet impinging on a flat plate. *International Communications in Heat and Mass Transfer*, 35(7), pp.873-880.
- Anderson. (2008). *Fluids lectures* (Vol. 17). MIT – Spring lecture series.
- ANSYS Inc. (2021). ANSYS CFX solver theory guide. ANSYS, Inc., Canonsburg, PA.
- ANSYS Inc. (2022). Ansys Granta Selector materials selection software <https://www.ansys.com/products/materials/granta-selector> [accessed: 16/12/2022]
- Araya, G., (2019). Turbulence Model Assessment in Compressible Flows around Complex Geometries with Unstructured Grids. *Fluids*, 4(2), p.81.
- Blazek, J. (2005). Introduction. In *Computational Fluid Dynamics: Principles and Applications* (pp. 1–4). Elsevier. <https://doi.org/10.1016/B978-008044506-9/50003-5>
- Brennen, C. (2006). *An Internet Book on Fluid Dynamics - California Institute of Technology* (Vol. 1).
- Chanson, H. (1996). Air Entrainment in Partially Filled Conduits. In *Air Bubble Entrainment in Free-Surface Turbulent Shear Flows* (pp. 144–152). Elsevier. <https://doi.org/10.1016/B978-012168110-4/50016-3>
- Christopher, R. and Blottner, F., (2006). Review and Assessment of Turbulence Models for Hypersonic Flows: 2D/Asymmetric Cases. *44th AIAA Aerospace Sciences Meeting and Exhibit*.
- DeSpirito, J., Edge, H., Weinacht, P., Sahu, J. and Dinavahi, S., (2000). Computational Fluid Dynamic (CFD) Analysis of a Generic Missile with Grid Fins. *ARMY RESEARCH LABORATORY*, 1.
- Fox, R. W., & McDonald, A. T. (1992). Fluid machines. Introduction to fluid mechanics. John Wiley, New York, 544-625.

- Finkbeiner, J., Dunlap, P., Steinetz, B. and Daniels, C., (2008). Review of Seal Designs on the Apollo Spacecraft. *Journal of Spacecraft and Rockets*, 45(5), pp.900-910.
- Hanjalić, K., & Launder, B. E. (1972). A Reynolds stress model of turbulence and its application to thin shear flows. *Journal of Fluid Mechanics*, 52(4), 609–638. <https://doi.org/10.1017/S002211207200268X>
- Maruyama, D., Kusunose, K., Matsushima, K. and Nakahashi, K., (2011). Aerodynamic analysis and design of Busemann biplane: towards efficient supersonic flight. *Proceedings of the Institution of Mechanical Engineers, Part G: Journal of Aerospace Engineering*, 226(2), pp.217-238.
- Menter, F. R. (1994). Two-equation eddy-viscosity turbulence models for engineering applications. *AIAA Journal*, 32(8), 1598–1605. <https://doi.org/10.2514/3.12149>
- Modesti, D., & Pirozzoli, S. (2016). Reynolds and Mach number effects in compressible turbulent channel flow. *International Journal of Heat and Fluid Flow*, 59, 33–49. <https://doi.org/10.1016/j.ijheatfluidflow.2016.01.007>
- NACA and NASA, (2017). *A study of NACA and NASA published information of pertinence in the design of light aircraft*. NASA Technical Reports.
- Schüle, E. and Guyot, D., (2006). Novel High-Performance Grid Fins for Missile Control at High Speeds: Preliminary Numerical and Experimental Investigations. *NATO*, 1, pp.12-15.
- Shahar. And Space X., (2020). GitHub repository, <https://github.com/shahar603/Telemetry-Data/tree/master/FormoSat-5>. [Accessed 18/10/2020].
- Sharma, N. and Kumar, R., (2019). Missile Grid Fins Analysis using Computational Fluid Dynamics: A Systematic Review. *INCAS BULLETIN*, 11(1), pp.151-169.
- Shuai, S., Wray, T. and Agarwal, R., (2017). Turbulence Modelling of High-Speed Compressible Flows. *55th AIAA Aerospace Sciences Meeting*.
- SpaceX, (2019). *Falcon 9 Grid fin installation*. [image].
- SpaceX, (2019). *Telemetry Data - FormoSat5*. [image].
- SpaceX, (2022). *Rideshare Program* - <https://www.spacex.com/rideshare/> [accessed: 12/12/2022]
- Srinivasan, R., Vijayan, V. and Sridhar, K., (2017). Computational Fluid Dynamic Analysis of Missile with Grid Fins. *Journal of Applied Fluid Mechanics*, 10(SI).
- Tekure, V., & Venkatasubbaiah, K. (2021). Effect of Mach number and plate thickness on the flow field and heat transfer characteristics of supersonic turbulent flow over a flat plate at different thermal boundary conditions. *European Journal of Mechanics - B/Fluids*, 88, 160–177. <https://doi.org/10.1016/j.euromechflu.2021.04.002>
- U.S AirForce, (2015)). *Grid fins extended - rear view of M.O.A.B.* [image].

Venditti, B., (2022). The cost of spaceflight: Before and after SpaceX. Visual capitalist - <https://www.visualcapitalist.com/the-cost-of-space-flight/>
[Accessed: 24/02/2022]

White, F., 2009. *Fluid mechanics*, 7th edition, McGraw-Hill, New York.

Winterwerp, J. C., & van Kesteren, W. G. M. (2004). *Boundary Layer Flow* (pp. 5–28). [https://doi.org/10.1016/S0070-4571\(04\)80003-7](https://doi.org/10.1016/S0070-4571(04)80003-7)